

# A GROMOS Parameter Set for Vicinal Diether Functions: Properties of Polyethyleneoxide and Polyethyleneglycol

Patrick F. J. Fuchs,<sup>†,‡,§,||,\*</sup> Halvor S. Hansen,<sup>⊥</sup> Philippe H. Hünenberger,<sup>⊥</sup> and Bruno A. C. Horta<sup>⊥</sup>

<sup>†</sup>INSERM, U665, F-75739 Paris, France

<sup>‡</sup>Univ Paris Diderot, Sorbonne Paris Cité, UMR\_S 665, F-75739 Paris, France

<sup>§</sup>Institut National de la Transfusion Sanguine, F-75739 Paris, France

<sup>||</sup>CNRS, Laboratoire d'Imagerie Paramétrique, UMR 7623, 75006 Paris, France

<sup>⊥</sup>Laboratory of Physical Chemistry, ETH Zürich, CH-8093 Zürich, Switzerland

**ABSTRACT:** An extension 53A6<sub>OXY+D</sub> to the GROMOS 53A6<sub>OXY</sub> force field is reported that includes an accurate description of the vicinal diether function. The calibration is based on the model compound 1,2-dimethoxyethane (DXE) and involves a fitting of the relevant torsional-energy parameters against quantum-mechanical (QM) rotational energy profiles for the OCCO and CCOC dihedral angles in vacuum, followed by a validation against experimental conformer populations in the pure liquid and in aqueous mixtures. A systematic comparison between the 53A6, 56A6<sub>CARBO</sub>, 53A6<sub>OXY</sub>, and 53A6<sub>OXY+D</sub> parameter sets is also performed in terms of these properties, as well as in terms of the thermodynamic properties of dimethylether (DME), diethylether (DEE), 1-methoxypropane (MPH), and DXE. Finally, the new parameter set is further validated in the context of polyethers, namely polyethyleneoxide (PEO) and polyethyleneglycol (PEG). The 53A6<sub>OXY+D</sub> set reproduces well the QM rotational profiles of DXE in vacuum (by calibration), the conformational populations of DXE in the pure liquid and in aqueous mixtures, and the experimental thermodynamic pure-liquid and (polar and nonpolar) solvation properties of DME, DEE, MPH, and DXE. In particular, it accounts appropriately for the *gauche*-effect, both in its solvent-independent stereoelectronic component and in its solvent-dependent dielectric-screening component. In contrast to 53A6<sub>OXY</sub>, it also suggests a higher affinity of DXE for water compared to octanol, in agreement with the experimental partition coefficient. In the context of aqueous polyethers, the calculated size (Flory) exponent ( $\nu_g = 0.61$ ) for the molecular-weight dependence of the radius of gyration and persistence length ( $L_p = 0.39 \pm 0.04$  nm) agree well with estimates based on experiment or previous simulations with other force fields. The simulations also suggest a picture of aqueous polyethers as “water sponges”, in which the diether function “adsorbs” an essentially constant number of water molecules corresponding to first-shell hydrogen-bonded saturation of its oxygen atoms, with a tendency to include other ether oxygen atoms along the chain in the second shell, resulting in “water bridging”.

## I. INTRODUCTION

The ether function (i.e., functional group) is one of the main chemical functions of organic chemistry, present in numerous technologically and biologically relevant molecules. Simple linear or cyclic mono- and diethers (Figure 1), such as dimethylether (DME), diethylether (DEE), 1-methoxypropane (MPH), 1,2-dimethoxyethane (DXE), tetrahydrofuran, tetrahydropyran, or dioxane, are commonly used in the chemical industry and in the laboratory as low-polarity solvents. The discovery of cyclic vicinal polyethers (crown ethers) also represented a tremendous step forward in coordination chemistry, resulting from their ability to form high-affinity complexes with metal cations that are soluble in low-polarity media.<sup>1,2</sup> These compounds are also thought nowadays to be promising antitumor agents.<sup>3</sup> In the living world, the ether function is present in all carbohydrates as well as in some lipids. In the context of carbohydrates, diether functions, either geminal (within the hemiacetal or acetal group) or vicinal (in a slightly disguised form, within the exocyclic hydroxymethyl group), represent a basic structural element of the furanose and pyranose rings. In the context of lipids, ether lipids<sup>4,5</sup> are ubiquitous in eukaryotic and prokaryotic biomembranes and may become a major component in some extremophile

bacteria.<sup>4</sup> They are also thought to act as second messengers and to play an antioxidant role.<sup>5</sup> In these lipids, an ether function is typically found as a replacement for the ester linkage connecting glycerol to one or both of the lipid tails *sn*-1 and *sn*-2 of a phospholipid. Plasmalogen is another important type of ether lipid,<sup>5</sup> in which the substitution involves a vinyl–ether linkage for the *sn*-1 chain. Finally, polymers involving successive vicinal diether functions (polyethers), such as polyethyleneoxide (PEO) and polyethyleneglycol (PEG), have attracted much interest in the recent years. In the literature, PEG is often used as a generic acronym for both types of molecules, irrespective of their molecular weight and the nature of their termini. However, a distinction is sometimes also made<sup>6</sup> between polymers with molecular weights below 20 kDa, referred to as PEG, polymers with higher weights, referred to as polyethyleneoxide (PEO), and polymers of any weight, referred to as polyoxyethylene (POE). In the present article, a slightly different nomenclature<sup>7</sup> is applied, distinguishing between polymer types based on the nature of their termini (Figure

**Special Issue:** Wilfred F. van Gunsteren Festschrift

**Received:** March 25, 2012

**Published:** June 18, 2012



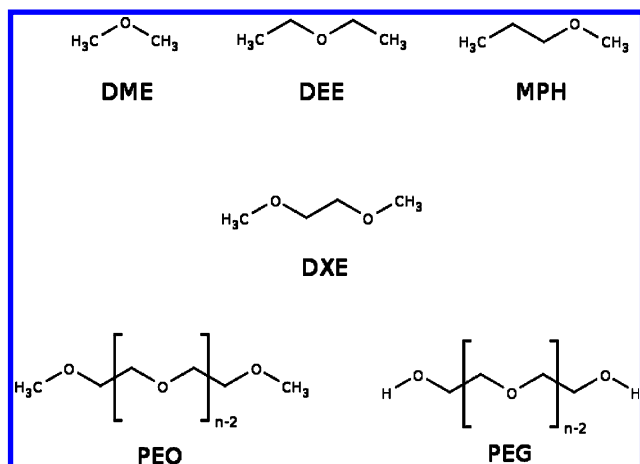


**Figure 1.** Chemical structures of the small mono- and diethers as well as of the longer polyethers considered in this work. For the small ethers, the same nomenclature is used as in ref 48: dimethylether (DME), diethylether (DEE), 1-methoxypropane (MPH), and 1,2-dimethoxyethane (DXE). The longer polyethers are polyethyleneoxide (PEO) and polyethyleneglycol (PEG). The two polymer types are distinguished here on the basis of the nature of their termini, namely hydroxy-terminated for PEG and methoxy-terminated for PEO. The degree of polymerization  $n$  corresponds to the number of oxygen atoms in the polymer, and polyethers with a specified  $n$  are noted here PEO $n$  or PEG $n$ .

1), namely, hydroxy-terminated polymers are referred to as PEG, and methoxy-terminated polymers are referred to as PEO. Polyethers are key components in a number of industrial (e.g., materials,<sup>8,9</sup> lubricants,<sup>10,11</sup> dispersants<sup>12</sup>), technological,<sup>13</sup> biotechnological, and biomedical<sup>6</sup> applications. Among these

applications, the ability of PEO or PEG to host biological material such as cells<sup>14</sup> or to enhance protein crystallization<sup>15,16</sup> can be cited. Chains of PEG can also be attached to different types of biomolecules (e.g., proteins, nucleic acids, lipids, drugs) in a process known as PEGylation.<sup>17</sup> The PEGylation of a molecule may be used to improve drug delivery<sup>17</sup> by protecting the molecule against enzymatic degradation, reducing its antigenicity, or increasing its solubility. Short stretches of polyethers are also involved in so-called PEG surfactants.<sup>18,19</sup> These are usually labeled C $_i$ E $_j$ , corresponding to an alkane chain of  $i$  carbon atoms, followed by a stretch of vicinal diether functions involving  $j$  oxygen atoms, and terminated by a hydroxyl group. These nonionic surfactants are used routinely for membrane-protein purification and crystallization, often together with a cosurfactant such as  $\beta$ -octylglucoside.<sup>18,19</sup>

Experimentally, the properties of polyethers can be investigated by a variety of spectroscopic techniques,<sup>20</sup> including light and neutron scattering, fluorescence spectroscopy, and nuclear magnetic resonance (NMR) spectroscopy. Among these, dynamic light scattering<sup>21</sup> is particularly useful, permitting an evaluation of the radius of gyration and of the persistence length of a polymer,<sup>22</sup> two central quantities for characterizing its shape in a statistical sense. The experimental investigation of polyether properties is nowadays usefully complemented (see references in Table 1) by molecular modeling techniques, including, in particular, atomistic molecular dynamics (MD) simulations, capable of providing information at spatial ( $\sim 0.1$  nm), temporal ( $\sim 1$  fs), and energetic (single-atom interactions) resolutions inaccessible to experiment. The price to pay for this impressive resolution is that the accuracy of a simulation is intrinsically limited by that

**Table 1.** Available Classical Force Fields for the Representation of Polyethyleneoxide (PEO) and Polyethyleneglycol (PEG)<sup>a</sup>

model	year	basis force field	type <sup>b</sup>	water model	ref
Smith <sup>c</sup>	1993		AA/NP	TIP4P <sup>128</sup>	67
	1998		AA/NP	TIP4P <sup>128</sup>	64
	2002		AA/NP	TIP4P <sup>128</sup>	68
	2011		AA/EP	SWM4-DP <sup>129</sup>	66
Thomas <sup>d</sup>	1994		AA/NP		70
Müller–Plathe <sup>e</sup>	1995	GROMOS 37C4 <sup>37</sup>	UA/NP		71,72
Tasaki <sup>f</sup>	1996	Smith model <sup>67</sup>	AA/NP	SPC <sup>93</sup>	69
Kolafa and Ratner <sup>g</sup>	1998		UA/EP		65
Anderson and Wilson	2004	OPLS-AA <sup>76</sup>	AA/NP	TIP4P <sup>128</sup>	75
	2005	OPLS-AA <sup>76</sup>	AA/NP	TIP4P <sup>128</sup>	74
C35r	2008	CHARMM C35 <sup>27</sup>	AA/NP	TIP3P <sup>128</sup>	7
Larson	2008	GROMOS 45A3 <sup>42</sup>	UA/NP	SPC <sup>93</sup>	52
Sadowski <sup>h</sup>	2008	TraPPE-UA <sup>78</sup>	UA/NP	TIP4P-EW <sup>130</sup>	77
56A6 <sup>CARBO</sup> <sup>i</sup>	2010	GROMOS 53A6	UA/NP	SPC <sup>93</sup>	47
Boutin <sup>j</sup>	2011	AUA4 <sup>80</sup>	UA/NP		79
Bunker	2011	OPLS-AA <sup>76</sup>	AA/NP	TIP3P <sup>128</sup>	81
Roccatano <sup>k</sup>	2011	GROMOS 53A6 <sup>82</sup> or OPLS-UA <sup>83</sup>	UA/NP	SPC <sup>93</sup> or SPC/E <sup>131</sup>	50

<sup>a</sup>For each model, the model name or author group, publication year, basis force field, force-field type, compatible water model and literature reference are indicated. <sup>b</sup>AA, all atom; UA, united atom; NP, non-polarizable, that is, implicit representation of electronic polarizability effects by means of charge enhancement; EP, explicit representation of electronic polarizability. <sup>c</sup>Probably the most frequently used to date, main successive revisions indicated, “standalone” force field (not inscribed in the framework of a general biomolecular force field). <sup>d</sup>Initially developed for PEO crystals (no associated water model). <sup>e</sup>Compatible with GROMOS, presumably the parameter set 37C4 (ref 37). <sup>f</sup>Smith model with modified charges. <sup>g</sup>Initially developed for gas-phase or pure-liquid simulations (no associated water model). <sup>h</sup>TraPPE-UA with modified nonbonded interactions based on Anderson and Wilson. <sup>i</sup>Most recent GROMOS parameter set for hexopyranose-based carbohydrates (mentioned here owing to its relevance for the present work). <sup>j</sup>Transferable force field aimed at reproducing phase-equilibrium and interfacial properties of liquid–vapor systems (no associated water model). <sup>k</sup>Claimed to be compatible with GROMOS, presumably the parameter set 53A6 (ref 82), or with OPLS-UA (ref 83), as well as with either the SPC or the SPC/E water model, so far only available for DXE. See ref 133 for the extension to PEO and PEG.

of the underlying computational model (classical approximation, force-field functional form and parameters, accessible system size and time scale, and employed simulation methodology).

The main classical force fields for (bio)molecular simulation such as CHARMM,<sup>23–27</sup> AMBER,<sup>28–31</sup> OPLS,<sup>32–35</sup> or GROMOS<sup>36–49</sup> include parameters for the ether function and are typically able to reproduce the main thermodynamic and dynamic properties of simple monoethers such as DME or DEE (Figure 1) with a reasonable accuracy, in the liquid phase as well as in aqueous solution. However, the direct transfer of these parameters to compounds involving vicinal diether functions, such as DXE, PEO, and PEG (Figure 1), or carbohydrates, leads to a relatively inaccurate description.<sup>47,50–52</sup> The main reason for this lack of transferability is related to the so-called *gauche*-effect,<sup>51,53–63</sup> namely, a stereo-electronically induced preference of the OCCO dihedral angle of a vicinal diether for the two *gauche* over the *trans* configuration, although the latter would *a priori* appear to be favored in terms of bond-dipole and steric interactions. In aqueous solution, high dielectric screening as well as specific hydration (water bridging) may also add up to the purely stereoelectronic *gauche*-effect.<sup>51,64</sup> As a result, the appropriate calibration of the vicinal diether function within a classical force field requires an additional parametrization step subsequent to that of the monoether function. This step mainly concerns the OCCO torsional-energy parameters and, possibly, the corresponding oxygen–oxygen third-neighbor nonbonded interaction parameters, the latter encompassing the oxygen–oxygen 1,4-Lennard-Jones (dispersion and repulsion) and 1,4-electrostatic (repulsion, given the identical partial charges of the oxygen atoms) interactions.

This requirement has been realized previously, and Table 1 presents a (probably nonexhaustive) list of studies that have aimed at a proper representation of the vicinal diether function, predominantly in the framework of one of the main (bio)molecular force fields, and with the goal of investigating the properties of PEO and PEG. Note that carbohydrate force fields have been omitted from this list, although they typically also involve a careful consideration of the OCCO parameters in the specific context of the exocyclic hydroxymethyl group attached to furanose or pyranose rings. One exception is the GROMOS 56A6<sub>CARBO</sub> force field,<sup>47</sup> which is of special relevance for the present work. All but two<sup>65,66</sup> of the proposed models are nonpolarizable, that is, involve an implicit representation of electronic polarizability effects by means of charge enhancement.

Among the models listed in Table 1, the Smith force field<sup>64,66–68</sup> is the oldest (1993) and probably the most frequently used to date. It was refined over the years to improve its agreement with experimental thermodynamic properties<sup>68</sup> and, more recently, to explicitly account for electronic polarizability.<sup>66</sup> The Tasaki model<sup>69</sup> is a variant of the Smith force field, with partial charges readjusted based on simulations of PEO in water. The Thomas model<sup>70</sup> was derived considering the properties of PEO crystals. The Müller-Plathe model<sup>71,72</sup> is compatible with GROMOS, presumably the parameter set 37C4,<sup>37</sup> and was designed on the basis of quantum-mechanical (QM) calculations for DXE,<sup>73</sup> with the aim of simulating PEO in the presence of lithium ions at high temperature. The Kolafa and Ratner<sup>65</sup> model is the oldest explicitly polarizable model and was designed considering density, dipole moments, dielectric constant, and QM calculations. The Anderson and

Wilson model<sup>74,75</sup> is compatible with OPLS-AA,<sup>76</sup> and was designed by recalibration of the OCCO torsional-energy parameters against the results of QM calculations in the context of DXE. The force-field parameters of CHARMM for linear and cyclic monoethers were revised in 2007, leading to the set labeled C35.<sup>27</sup> To extend the description to diethers, the OCCO torsional-energy parameters were subsequently refined against QM data in the context of DXE, leading to a new set labeled C35r.<sup>7</sup> This model was validated in simulations of aqueous PEO and found to reproduce very well a number of important experimental properties (dependence of the radius of gyration on the molecular weight, persistence length, hydrodynamic radius, and shape anisotropy). The Larson model,<sup>52</sup> compatible with GROMOS 45A3<sup>42</sup> and involving modified nonbonded interaction parameters for the ether oxygen atom and OCCO torsional-energy parameters, was applied to study the interaction between PEO and sodium dodecyl sulfate (SDS) micelles. The Sadowski model<sup>77</sup> represents a modified version of the TraPPE-UA united-atom force field for ethers<sup>78</sup> based on the OCCO torsional-energy parameters developed earlier by Anderson and Wilson, and was applied in aqueous PEO simulations. The Boutin model<sup>79</sup> is compatible with the AUA4 force field<sup>80</sup> and was designed for the study of phase-equilibrium and interfacial properties of liquid–vapor systems. The Bunker model,<sup>81</sup> compatible with OPLS-AA,<sup>76</sup> was developed for the investigation of PEGylated lipid bilayers. Finally, very recently, Roccatano and co-workers<sup>50</sup> proposed a new united-atom model for DXE, which is compatible with GROMOS, presumably the parameter set 53A6<sup>82</sup> or OPLS-UA.<sup>83</sup> The GROMOS 56A6<sub>CARBO</sub> force field,<sup>47</sup> also mentioned in Table 1 owing to its relevance for the present work, is compatible with GROMOS 53A6 as well, and results from a complete reoptimization of the parameters relevant for hexopyranose-based carbohydrates against available experimental data. Note, however, that this parameter set is still meant to be generally applicable to all compounds of the elements C, H, and O, excluding double bonds and rings other than six-membered rings.<sup>47</sup>

The GROMOS force field<sup>36–49,82,84–88</sup> (see also [www.gromos.net](http://www.gromos.net)) is one of the main classical united-atom and nonpolarizable force fields for (bio)molecular systems. It encompasses parameters for all chemical functions relevant for the simulations of proteins and nucleic acids, as well as the most common carbohydrates and lipids. This force field has evolved over the years, the main releases being 26C1 (1984, ref 36), 37C4 (1987; ref 37), 43A1 (1996; refs 38 and 39), 43A2 (2000; ref 40), 45A3 (2001; ref 42), 45A4 (2005; refs 43–46), 53A5 (2004; ref 82), 53A6 (2004; ref 82), and 54A7 (2011; ref 49). None of these versions includes a specific parametrization for vicinal diether functions, although some were proposed independently.<sup>47,50,52,58,71,72</sup> In 2009, Winger et al.<sup>89</sup> compared the performances of different released versions of the GROMOS force field up to 53A6 in the context of short PEO molecules in water. It was suggested that the relatively low partial charge used in the 53A6 parameter set<sup>82</sup> for the ether oxygen atom was inducing too compact conformations, resulting from an underestimation of the hydration free energy. Recently, a new version of the GROMOS force field referred to as 53A6<sub>OXY</sub> was introduced<sup>48</sup> that includes an improved description of the most common oxygen-containing chemical functions, namely, alcohols, ethers, aldehydes, ketones, carboxylic acids, and esters (see also ref 90 for an extension 53A6<sub>OXY+A</sub> including the amide function). The calibration

Table 2. Overview of the Simulations Performed in This Work<sup>a</sup>

system content	$N_{\text{rep}}^b$	$t_{\text{sim}}^c$ (ns)	$T_{\text{sim}}^d$ (K)	solvent	$N_{\text{svt}}^e$	$L^f$ (nm)		
DME	1	1.9	254	DME liquid <sup>g</sup>	512	3.80		
	1	9.9	254	vacuum <sup>g</sup>				
	3	2	300	water <sup>h</sup>	893	3.00		
	3	2	300	cyclohexane <sup>h</sup>	262	3.76		
	3	2	300	vacuum <sup>h</sup>				
DEE	1	1.9	300	DEE liquid <sup>g</sup>	500	4.46		
	1	9.9	300	vacuum <sup>g</sup>				
	3	2	300	water <sup>h</sup>	966	3.10		
	3	2	300	cyclohexane <sup>h</sup>	262	3.76		
	3	2	300	vacuum <sup>h</sup>				
MPH	1	1.9	300	MPH liquid <sup>g</sup>	500	4.45		
	1	9.9	300	vacuum <sup>g</sup>				
	3	2	300	water <sup>k</sup>	966	3.10		
	3	2	300	cyclohexane <sup>h</sup>	262	3.76		
	3	2	300	vacuum <sup>h</sup>				
DXE	1	1.9	300	DXE liquid <sup>g</sup>	256	3.59		
	1	9.9	300	vacuum <sup>g</sup>				
	3	2	300	water <sup>h</sup>	966	3.10		
	3	2	300	cyclohexane <sup>h</sup>	262	3.76		
	3	2/20 <sup>l</sup>	300	octanol <sup>h</sup>	256	4.09		
	3	2	300	vacuum <sup>h</sup>				
DXE 1.0/water 0.0	1	9	318	DXE liquid <sup>k</sup>	300 DXE	3.80		
DXE 0.6/water 0.4	1	9	318	DXE/water <sup>k</sup>	300 DXE + 200 SPC	3.93		
DXE 0.3/water 0.7	1	9	318	DXE/water <sup>k</sup>	300 DXE + 700SPC	3.80		
DXE 0.001/water 0.999 <sup>m</sup>	1	299	318	water	966	3.10		
system content	$N_{\text{rep}}$	$t_{\text{sim}}^c$ (ns)	$T_{\text{sim}}^d$ (K)	$N_{\text{pol}}^i$	$N_{\text{sol}}^j$	solvent	$N_{\text{svt}}^e$	$L^f$ (nm)
PEO <sup>n</sup>	3	300	296	10	30	water	2900	4.47
	3	300	296	19	57	water	2900	4.49
	6	300	296	28	84	water	5000	4.49
(LS) <sup>o</sup>	1	300	296	28	84	water	5000	5.37
	3	300	296	37	111	water	6500	5.87
PEG <sup>n</sup>	3	300	296	28	84	water	5000	5.37

<sup>a</sup>All simulations (except in vacuum) were carried out at a pressure of 1 bar. See Section II for details. <sup>b</sup>Number of independent repeats of the simulation with different initial velocities ( $N_{\text{rep}}$ ). <sup>c</sup>Duration of the simulation after equilibration ( $t_{\text{sim}}$ ; for free-energy calculations, this is the duration per  $\lambda$ -point). <sup>d</sup>Simulation temperature ( $T_{\text{sim}}$ ). <sup>e</sup>Number of solvent molecules ( $N_{\text{svt}}$ ). <sup>f</sup>Average box edge length ( $L$ ). <sup>g</sup>These simulations were performed for calculating  $\rho_{\text{liq}}$  and  $\Delta H_{\text{vap}}$ . <sup>h</sup>These simulations were performed for calculating  $\Delta G_{\text{wat}}$  and  $\Delta G_{\text{che}}$  and involved the decoupling of a single solute molecule in the indicated solvent (along with a corresponding calculation in vacuum, 2 ns per  $\lambda$ -point, not indicated explicitly in the table). <sup>i</sup>Degree of polymerization ( $N_{\text{pol}}$ ). <sup>j</sup>Number of solute atoms ( $N_{\text{sol}}$ ). <sup>k</sup>These simulations were performed for calculating conformer populations of DXE in the pure liquid and in aqueous mixtures. <sup>l</sup>Duration 20 ns at  $\lambda = 0$  and  $\lambda = 0.05$  for the electrostatic decoupling in octanol, 2 ns otherwise. <sup>m</sup>This system corresponds to 1 DXE molecule in pure water, and aims at mimicking an infinite-dilution situation. <sup>n</sup>These simulations involved a single PEO or PEG molecule in water. <sup>o</sup>All simulations were performed using a reaction field (RF) scheme for electrostatic interactions, except for this single simulation, performed using a lattice-sum (LS) scheme (PME) for comparison.

relied on the optimization of simulated pure-liquid (density  $\rho_{\text{liq}}$  and enthalpy of vaporization  $\Delta H_{\text{vap}}$ ) as well as solvation (free energies of solvation in water  $\Delta G_{\text{wat}}$  and cyclohexane  $\Delta G_{\text{che}}$ ) properties against experimental data for 35 organic liquids, including four ethers (DME, DEE, MPH, and DXE; Figure 1). In agreement with the suggestion of Winger et al.,<sup>89</sup> a charge increase of the ether oxygen atom relative to the 53A6 version (from  $-0.324$  to  $-0.580 e$ ), along with a readjustment of the Lennard-Jones interaction parameters for the corresponding atom type OE, were found necessary to improve the agreement with experiment in terms of  $\Delta G_{\text{wat}}$  (root-mean-square deviation over the four ethers reduced from 11.7 to 2.1 kJ mol<sup>-1</sup>). Note that Roccatano and co-workers<sup>50</sup> independently arrived at the same conclusion, and also increased the partial charge of the ether oxygen atom (to  $-0.450 e$ ). As discussed above, however, an appropriate calibration for monoethers is not a sufficient condition to ensure the accurate description of vicinal diethers. Indeed, detailed analysis of the conformational properties of

DXE as well as preliminary simulations of PEO chains using 53A6<sub>OXY</sub> (unpublished results) revealed important discrepancies with respect to experimental data.

The goal of the present work is to adjust the 53A6<sub>OXY</sub> force field for the accurate description of vicinal diethers. The reoptimization is based on the compound DXE (Figure 1) and involves a fitting of the relevant torsional-energy parameters against QM rotational energy profiles in vacuum,<sup>27</sup> followed by a validation against experimental conformer populations in the pure liquid as well as in two aqueous mixtures, inferred from Raman spectroscopy measurements.<sup>91</sup> The resulting parameter set is labeled 53A6<sub>OXY+D</sub>, where the “D” stands for “diether”. A systematic comparison between the 53A6, 56A6<sub>CARBO</sub>, 53A6<sub>OXY</sub>, and 53A6<sub>OXY+D</sub> sets is also performed in terms of these properties, as well as in terms of the thermodynamic pure-liquid and (polar and nonpolar) solvation properties of the mono- and diethers DME, DEE, MPH, and DXE. Finally,



the 53A6<sub>OXY+D</sub> parameter set is further validated in the context of polyethers, namely, PEO and PEG.

The ultimate goal of this development work is to produce a parametrization of vicinal diethers, including PEO and PEG, that it is fully compatible with the 53A6<sub>OXY</sub> force field (and its subsequent extension to amides,<sup>90</sup> as well as to other nitrogen compounds, sulfur compounds, and aromatic alcohols; work in progress) and the rest of the GROMOS force field for biomolecules (proteins, nucleic acids, lipids, and carbohydrates). This compatibility is particularly important considering the relevance of PEO- or PEG-hosted and of PEGylated biomolecules. Although previous studies have suggested such GROMOS compatible sets,<sup>47,50,52,71,72</sup> these were designed for previous versions of the force field (37C4, 45A3, or 53A6), where it is noted that, considering the versions of the GROMOS force field since 2004, the changes from 45A4 to 53A5, from 53A5 to 53A6 and from 53A6 to 53A6<sub>OXY</sub> are extensive, the latter especially for oxygen-containing compounds such as ethers, while those from 53A6 to 54A7 are comparatively more limited, affecting only the backbone of peptides and the headgroup of phosphatidylcholine lipids. The 56A6<sub>CARBO</sub> set is also considered in the present work, in view of a subsequent merging of this carbohydrate-specific force field into 53A6<sub>OXY</sub>. In this context, the consideration of cyclic ethers, which are left out in the present work, will also become very important.

## II. COMPUTATIONAL DETAILS

**II.1. Simulation Parameters.** All MD simulations were performed using the GROMACS 4.0.7 program,<sup>92</sup> considering four variants of the GROMOS force field along with the SPC water model.<sup>93</sup> The parameter sets considered are 53A6,<sup>82</sup> 56A6<sub>CARBO</sub>,<sup>47</sup> 53A6<sub>OXY</sub>,<sup>48</sup> and 53A6<sub>OXY+D</sub>, the latter set being the one specifically reoptimized for vicinal diether functions in the present study (Section II.2).

The equations of motion were integrated using the leapfrog algorithm<sup>94</sup> based on a 2 fs time step. The solute bond-length distances were constrained by application of the P-LINCS algorithm,<sup>95</sup> and the full rigidity of the water molecules was enforced by means of the SETTLE algorithm.<sup>96</sup> Except for the simulations in vacuum (Section II.3), periodic boundary conditions were applied based on cubic computational boxes. Unless otherwise specified, the simulations were carried out at constant temperature and pressure, thermostating and barostating relying on the Berendsen weak-coupling approach.<sup>97</sup> In this case, the temperature was maintained close to its reference value  $T$  (254, 296, 300, or 318 K, depending on the system considered) by means of a weak-coupling thermostat with a relaxation time of 0.1 ps, while the pressure was maintained close to a reference value  $P = 1$  bar by means of a weak-coupling barostat (isotropic coordinate scaling) with a relaxation time of 1 ps. For all simulations, the isothermal compressibility for the barostat was set to the experimental value for water<sup>98,99</sup> ( $\beta_{\text{wat}} = 4.5 \times 10^{-5} \text{ bar}^{-1}$  at 300 K and 1 bar), except for the simulations in cyclohexane, for which the experimental value for this solvent<sup>100</sup> ( $\beta_{\text{che}} = 11.2 \times 10^{-5} \text{ bar}^{-1}$  at 300 K and 1 bar) was used instead.

For all but one simulation, the electrostatic interactions were handled using a twin-range scheme, with short- and long-range cutoff distances set to 0.8 and 1.4 nm, respectively, and a frequency of 5 timesteps for the update of the short-range pairlist and intermediate-range interactions. The mean effect of the omitted long-range interactions was reintroduced by means

of a reaction-field (RF) correction.<sup>101</sup> The corresponding RF dielectric permittivities were set to 6.2 (DME), 4.2 (DEE), 4.2 (MPH), or 7.3 (DXE) for the pure liquids (same values as in ref 48, based on ref 102), or to an intermediate value interpolated linearly between that of the pure liquid and that of the SPC water model<sup>103</sup> (61) for the liquid mixtures. A single lattice-sum (LS) simulation was also performed for PEO28. In this case, the particle-mesh Ewald (PME) scheme<sup>104,105</sup> was applied, with a cutoff distance of 1.0 nm, a grid spacing of 0.12 nm and an interpolation scheme of order 4.

Specifics of the simulations involved in the parametrization of the vicinal diether function for 53A6<sub>OXY+D</sub> based on DXE, in the comparison of the 53A6, 56A6<sub>CARBO</sub>, 53A6<sub>OXY</sub>, and 53A6<sub>OXY+D</sub> parameter sets concerning the thermodynamic properties of small mono- and diethers (DME, DEE, MPH, and DXE), and in the validation of the 53A6<sub>OXY+D</sub> parameter set in the context of polyethers (PEO, PEG), are provided in Sections II.2, II.3, and II.4, respectively. An overview of all the simulations performed in this work is available in Table 2.

### II.2. Parametrization of the Vicinal Diether Function.

The adjustment of the 53A6<sub>OXY</sub> parameter set<sup>48</sup> into set 53A6<sub>OXY+D</sub> encompassing an improved description of the vicinal diether function involved a reoptimization of the torsional energy parameters for the dihedrals of types OCCO (the one affected by the *gauche*-effect<sup>51,53–63</sup>) and CCOC (equally relevant for the PEO and PEG chains, as well as the PEO termini). A change in the corresponding third-neighbor Lennard-Jones interaction parameters was envisioned but ultimately found to be unnecessary. The third-neighbor electrostatic interaction parameters, controlled by the partial charges of the corresponding atoms, were also kept unaltered relative to 53A6<sub>OXY</sub> (assumption of transferability for the atomic partial charges from mono- to diether functions). No adjustment was undertaken for the dihedral of type CCOH (relevant for the PEG termini), considering its limited influence on the properties of PEG and the omnipresence of this term in other (bio)molecules, suggesting an already appropriate parametrization within GROMOS.

The reoptimization was based on the compound DXE (Figure 1) and involved a fitting of the OCCO and CCOC torsional-energy parameters against QM rotational energy profiles in vacuum, calculated at the MP2/cc-pVTZ/MP2/6-31G(d) level of theory,<sup>27</sup> followed by a validation against experimental conformer populations in the pure liquid as well as in two aqueous mixtures, inferred from Raman spectroscopy measurements.<sup>91</sup> For comparison purposes, the 53A6, 56A6<sub>CARBO</sub>, and 53A6<sub>OXY</sub> parameter sets were also assessed against the same data.

The compound DXE involves three successive dihedral angles, of types CCOC, OCCO, and CCOC, respectively (the acronym CCOC is also used for the topologically equivalent COCC quadruplet). Considering the *gauche* plus ( $G^+$ , or simply  $G$ ,  $60^\circ$ ), *trans* ( $T$ ,  $180^\circ$ ), and *gauche* minus ( $G^-$ ,  $-60^\circ$ ) conformations of these three dihedral angles, this molecule presents 27 conformers with the three bonds in a staggered configuration. However, as summarized in Table 3, a number of these conformers is equivalent by inversion of the atom numbering or enantiomers of each others, reducing the number of energetically distinct classes of conformers to 10.

For the optimization of the OCCO and CCOC torsional-energy parameters against QM rotational energy profiles for DXE in vacuum, the dihedral angle  $X$  under consideration was altered in increments of  $15^\circ$ , with the two other dihedral angles

**Table 3. Definition of the 10 Energetically Distinct Classes of Conformers for 1,2-Dimethoxyethane (DXE)<sup>a</sup>**

name	conformers in the group
TTT	TTT
TGT	TG–T # TG+T
TGG'	(G–G+T = TG+G–) # (G+G–T = TG–G+)
TTG	(G–TT = TTG–) # (G+TT = TTG+)
TGG	(G–G–T = TG–G–) # (G+G+T = TG+G+)
GTG	G–TG– # G+TG+
GTG'	(G–TG+ = G+TG–)
GGG	G–G–G– # G+G+G+
G'GG'	G–G+G– # G+G–G+
GGG'	(G–G+G+ = G+G+G–) # (G+G–G– = G–G–G+)

<sup>a</sup>Considering *gauche* plus (G+, 60°), *trans* (T, 180°), and *gauche* minus (G–, –60°) conformations of the three successive dihedral angles (CCOC, OCCO, and CCOC), there are 27 conformers with the three bonds in a staggered configuration. A number of these conformers are equivalent by inversion of the atom numbering (equal sign) or enantiomers of each other (hash sign), reducing the number of energetically distinct classes of conformers to the 10 classes listed here. The naming of these classes follows that introduced in ref 132 for ethylene glycol, whereby a prime indicates that two G that follow each other have an opposite sign.

held at a fixed value. The configurations considered here were TXT or GXT for OCCO and TTX for CCOC. At each point, the configuration was relaxed by steepest-descent energy minimization with strong restraints on the three dihedral angles (force constant  $10^4$  kJ mol<sup>–1</sup> rad<sup>–2</sup>). The difference between the QM energy profile and the corresponding classical profile (excluding the restraint energy and the torsional potential energy for the dihedral angle X under consideration) was then fitted to a cosine series including terms of multiplicities 1, 2, and 3 by means of a nonlinear least-squares fitting procedure. The resulting reoptimized parameters can be found in Table 4.

For the validation against experimental conformer populations in pure-liquid or aqueous DXE inferred based on Raman spectroscopy, simulations of DXE at four hydration levels (mole fractions 0.3, 0.6, and 1.0 of DXE) were performed at the experimental temperature of 318 K, for a duration of 9 ns after 1 ns equilibration (Table 2). The assignment of trajectory configurations to the 10 energetically distinct classes of conformers (Table 3) relied on intervals of  $\pm 60^\circ$  centered at 60°, 180° or –60° for the attribution of each dihedral angle to the G+, T, and G– wells, respectively. An additional simulation at mole fraction 0.001 was also undertaken to mimic an infinite-dilution situation. This simulation was extended to 299 ns, so as to improve the statistics concerning the single DXE molecule in the system.

**II.3. Thermodynamic Properties of Small Mono- And Diethers.** The thermodynamic properties of the small mono- and diethers DME, DEE, MPH, and DXE (Figure 1) as calculated using the S3A6, S6A6<sub>CARBO</sub>, S3A6<sub>OXY</sub>, and S3A6<sub>OXY+D</sub> parameter sets were compared to each other and to experiment, see also Section II.2 for the corresponding comparison in terms of QM rotational profiles for DXE in vacuum and conformer populations for pure-liquid or aqueous DXE. For the ease of reference, the relevant parameters of the four force-field versions are listed in Tables 4 and 5. The thermodynamic properties considered include the pure-liquid density  $\rho_{\text{liq}}$  and enthalpy of vaporization  $\Delta H_{\text{vap}}$ , as well as the solvation free energies  $\Delta G_{\text{wat}}$  and  $\Delta G_{\text{che}}$  in water and in

cyclohexane, respectively. For DXE, the solvation free energy  $\Delta G_{\text{ol}}$  in octanol was also calculated. Note that all solvation free energies reported in this work (experimental and calculated) pertain to a point-to-point solvation process (transfer of the molecule from a fixed point in vacuum to a fixed point in solution). This is equivalent to a standard-state definition implying identical reference concentrations in the gas and solution phases (rather than, for example, a reference pressure of 1 bar in the gas phase and a reference molality of 1 mol kg<sup>–1</sup> in solution).

For the determination of  $\rho_{\text{liq}}$  and  $\Delta H_{\text{vap}}$ , pure-liquid simulations of the four ethers were performed at 300 K (or 254 K, i.e. the boiling point, for DME), for systems comprising 256–512 molecules and for durations of 1.9 ns after 0.1 ns equilibration (Table 2). These simulations relied on a stochastic thermostat<sup>106</sup> with a friction coefficient of 0.1 ps<sup>–1</sup> and a Parrinello–Rahman barostat<sup>107</sup> with a relaxation time of 4 ps (instead of the weak-coupling thermostat and barostat; Section II.1). For the determination of  $\Delta H_{\text{vap}}$ , vacuum simulations were required as well. These were performed at 300 K (or 254 K for DME), for a single molecule and for durations of 9.9 ns after 0.1 ns equilibration (Table 2). They also relied on a stochastic thermostat<sup>106</sup> (same friction coefficient, no barostat). As in ref 48, the enthalpy of vaporization  $\Delta H_{\text{vap}}$  was then calculated as the difference between the average potential energy of the molecule in vacuum and the average potential energy per molecule in the pure liquid, expressed on a per mole basis and increased by  $RT$ , where  $R$  is the ideal-gas constant and  $T$  is the absolute temperature.

The determination of  $\Delta G_{\text{wat}}$  and  $\Delta G_{\text{che}}$  (and  $\Delta G_{\text{ol}}$  for DXE) relied on pairs of thermodynamic integration<sup>108</sup> (TI) calculations, in vacuum and in solution, where the nonbonded interactions of the molecule (electrostatic and Lennard-Jones) were progressively removed, from full interaction to none, by means of a coupling parameter  $\lambda$ . A soft-core coupling scheme was employed, with a coupling exponent  $n = 1$ , a Lennard-Jones softness parameter  $\alpha_{\text{LJ}} = 0.5$ , and a soft-radius  $\sigma_{\text{H}} = 0.3$  nm for hydrogen atoms.<sup>109</sup> The TI calculations relied on 21 equally spaced (vacuum, cyclohexane) or 27 unequally spaced (water, more points close to  $\lambda = 0$ )  $\lambda$ -points. For DXE in octanol, the removal of electrostatic and Lennard-Jones interactions was performed in two successive TI calculations (21 and 22  $\lambda$ -points, respectively, in the latter case unequally spaced with more points around  $\lambda = 0.875$ ). The TI calculations in solution were performed at 300 K, for systems comprising 256–966 solvent molecules and involved 2 ns sampling per  $\lambda$ -point (Table 2). These simulations relied on a stochastic thermostat<sup>106</sup> with a friction coefficient of 0.1 ps<sup>–1</sup>. They were performed at constant volume, after 30 ps constant-pressure (weak-coupling barostat<sup>97</sup> with a relaxation time of 0.5 ps) equilibration of the volume at each  $\lambda$ -point. For DXE in octanol, the  $\lambda = 0$  and  $\lambda = 0.05$  points of the electrostatic decoupling required longer sampling (20 ns), due to the occurrence of a slow two-state process related to peculiar solute–solvent hydrogen bonding. The TI calculations in vacuum (not listed explicitly in Table 2) were performed at 300 K and involved 2 ns sampling per  $\lambda$ -point. They also relied on a stochastic thermostat<sup>106</sup> (same friction coefficient, no barostat). The solvation free energy was then calculated as the difference between the free energy of decoupling in vacuum and in the solvent. The two values were obtained by numerical integration (trapezoidal rule) of the derivative of the Hamiltonian with

Table 4. Covalent Interaction Parameters Used in Different GROMOS Force-Field Versions<sup>a</sup>

bond stretching	53A6	56A6 <sub>CARBO</sub>	53A6 <sub>OXY</sub>	53A6 <sub>OXY+D</sub>	type code <sup>b</sup>	<i>b</i> <sub>o</sub> (nm)	<i>k</i> <sub>b</sub> (10 <sup>6</sup> kJ mol <sup>−1</sup> nm <sup>−4</sup> )	
C–C	×	×	×	×	gb 27	0.153	7.15	
					gb 26	0.152	5.43	
C–O	×	×	×	×	gb 13	0.136	10.2	
					gb 20	0.1435	6.10	
O–H	×	×	×	×	gb 18	0.143	8.18	
					gb 1	0.100	15.7	
bond-angle bending	53A6	56A6 <sub>CARBO</sub>	53A6 <sub>OXY</sub>	53A6 <sub>OXY+D</sub>	type code <sup>b</sup>	<i>θ</i> <sub>o</sub> (deg)	<i>k</i> <sub>θ</sub> (kJ mol <sup>−1</sup> )	
C–C–O	×	×	×	×	ga 15	111.0	530.0	
					ga 9	109.5	320.0	
C–O–C	×	×	×	×	ga 15	111.0	530.0	
					ga 10	109.5	380.0	
C–O–H	×	×	×	×	ga 12	109.5	450.0	
C–C–C	×	×	×	×	ga 15	111.0	530.0	
dihedral-angle torsion	53A6	56A6 <sub>CARBO</sub>	53A6 <sub>OXY</sub>	53A6 <sub>OXY+D</sub>	type code <sup>b</sup>	<i>k</i> <sub>φ,<i>n</i></sub> (kJ mol <sup>−1</sup> )	cos <i>δ</i> <sub>φ,<i>n</i></sub>	<i>m</i> <sub>φ,<i>n</i></sub>
C–C–O–C	×	×	×	×	gd 23	1.260	+1	3
					<i>T</i> 2	4.900	+1	3
					<i>D</i> 1 <sup><i>d</i></sup>	<b>0.931</b>	−1	<b>1</b>
					<i>D</i> 2 <sup><i>d</i></sup>	<b>0.569</b>	+1	<b>2</b>
					<i>D</i> 3 <sup><i>d</i></sup>	<b>4.682</b>	+1	<b>3</b>
					gd 34 <sup><i>e</i></sup>	5.920	+1	3
O–C–C–O	×	×	×	×	<i>T</i> 12 <sup><i>f,g</i></sup>	4.500	−1	1
					<i>D</i> 4 <sup><i>d</i></sup>	<b>6.942</b>	−1	<b>1</b>
					<i>D</i> 5 <sup><i>d</i></sup>	<b>3.312</b>	+1	<b>2</b>
					<i>D</i> 6 <sup><i>d</i></sup>	<b>6.787</b>	+1	<b>3</b>
					gd 23	1.260	+1	3
					<i>T</i> 3	2.400	+1	3

<sup>a</sup>The parameter sets considered are 53A6<sup>82</sup>, 56A6<sub>CARBO</sub><sup>47</sup>, 53A6<sub>OXY</sub><sup>48</sup>, and 53A6<sub>OXY+D</sub> (this work). Only the parameters relevant for the compounds of Figure 1 are reported. They include the reference bond length  $b_o$  and force constant  $k_b$  for bond stretching, the reference bond angle  $\theta_o$  and force constant  $k_\theta$  for bond-angle bending, and the multiplicity  $m_{\phi,n}$ , phase-shift cosine  $\cos \delta_{\phi,n}$  and force constant  $k_{\phi,n}$  for dihedral-angle torsion (sum of terms  $n$ ). The functional forms of the corresponding terms are described in refs 39 and 41, namely  $(1/4)k_b(b^2 - b_o^2)^2$  for bond stretching,  $(1/2)k_\theta(\cos \theta - \cos \theta_o)^2$  for bond-angle bending, and  $k_{\phi,n}[1 + \cos \delta_{\phi,n} \cos(m_{\phi,n}\phi)]$  for dihedral-angle torsion. A cross (×) indicates lines applicable to a specific parameter set. <sup>b</sup>The type codes of the terms refer to the official interaction-function parameter (ifp) file of the GROMOS 53A6 force field (gb, bond parameter list; ga, angle-parameter list; gd, dihedral-parameter list) with the addition of the new dihedral-angle type codes (in italics) for 56A6<sub>CARBO</sub> (terms “T” referring to Table 6 in ref 47) and for 53A6<sub>OXY+D</sub> (terms “D”, in boldface). <sup>c</sup>In 56A6<sub>CARBO</sub>, this term is associated with  $\theta_o = 109.5$  deg and  $k_\theta = 285$  kJ mol<sup>-1</sup> (ga 8) for C–C–C in six-membered rings, and was adjusted here to the 53A6 parameters for C–C–C in linear chains. <sup>d</sup>The torsional-energy parameters optimized in this work are highlighted in boldface. <sup>e</sup>Equivalent to T1 in 56A6<sub>CARBO</sub>. <sup>f</sup>In 56A6<sub>CARBO</sub> this term is the *gauche*-effect term applied to the hydroxymethyl group (in addition to gd 34), another term (T13) applying within six-membered rings (see Table 6 in ref 47, irrelevant here). <sup>g</sup>In 56A6<sub>CARBO</sub> two additional terms (T10 and T11) also influence the rotation of the hydroxymethyl group (see Table 6 in ref 47), which are absent for ethers in chains.

respect to  $\lambda$ . All determination of  $\Delta G_{\text{wat}}$  and  $\Delta G_{\text{che}}$  (and  $\Delta G_{\text{otl}}$  for DXE) were repeated three times (Table 2) with different initial velocities, the corresponding average and standard deviation providing the final result and estimated error, respectively.

**II.4. Polyether Simulations.** The validation of the 53A6<sub>OXY+D</sub> parameter set in the context of polyethers involved simulations of one PEO or one PEG molecule solvated by 2900–6500 water molecules at 296 K (the same temperature as used in the simulations of ref 7) and were carried out for durations of 300 ns after 2 ns equilibration (Table 2). The oligomers considered were PEO10, PEO19, PEO28, PEO37, and PEG28, the number indicating the degree of polymerization (i.e., the number of oxygen atoms in the oligomer) (Figure 1). The effect of the degree of polymerization was not tested explicitly for PEG. Although the influence of the type of termini (methoxyl or hydroxyl) on polyethers can be important for short chains, especially in terms of hydration properties,<sup>110</sup> it has no significant influence on the polymer shape beyond a certain molecular weight.<sup>7</sup> Initial oligomer configurations were

generated using 2 ns stochastic dynamics simulation in vacuum, prior to solvation. For the ease of comparison, the numbers of water molecules in the different systems were chosen to be as close as possible to those employed in the PEO simulations of ref 7, except for PEO28, where the number had to be increased from 2900 to 5000 after the initial observation of direct interactions between the oligomer and its periodic copies. After this adjustment, artificial interactions between periodic copies presented a negligible occurrence (<1% of the trajectory configurations) for all the systems considered. In order to compare the effect of using RF vs LS electrostatics in the simulations (Section II.1), a single PEO28 simulation was carried out using LS electrostatics. Except for this LS simulation, all simulations were repeated 3–6 times (Table 2) with different initial velocities, so as to increase the statistics and obtain an indication of the uncertainty. The polyether simulations were analyzed in terms of the radius of gyration  $R_g$  and associated size exponent  $\nu_g$  of the persistence length  $L_p$ , and of the rotational autocorrelation functions  $C_r(t)$  and associated characteristic times  $\tau_r$ .

Table 5. Nonbonded Interaction Parameters Used in Different GROMOS Force-Field Versions<sup>a</sup>

normal LJ <sup>b</sup>	type	53A6	56A6 <sub>CARBO</sub>	53A6 <sub>OXY</sub>	53A6 <sub>OXY+D</sub>
$C_6^{1/2}$ (kJ mol <sup>-1</sup> nm <sup>12</sup> ) <sup>1/2</sup>	CH2	0.08642	0.08642	0.08642	0.08642
	CH2r	0.08564	0.08564	0.08564	0.08564
	CH3	0.09805	0.09805	0.09805	0.09805
	OE	0.04756	0.04756	0.04123	0.04123
	OA	0.04756	0.04756	0.04500	0.04500
	Or		0.04756		
	H	0	0	0	0
$C_{12,I}^{1/2}$ (10 <sup>-3</sup> [kJ mol <sup>-1</sup> nm <sup>12</sup> ] <sup>1/2</sup> )	CH2	5.828	5.828	5.828	5.828
	CH2r	5.297	5.297	5.297	5.297
	CH3	5.162	5.162	5.162	5.162
	OE	1.100	1.100	1.5297	1.5297
	OA	1.100	1.100	1.150	1.150
	Or		1.100		
	H	0	0	0	0
$C_{12,II}^{1/2}$ (10 <sup>-3</sup> [kJ mol <sup>-1</sup> nm <sup>12</sup> ] <sup>1/2</sup> )	CH2				
	CH2r				
	CH3				
	OE	1.227	1.227	1.5297	1.5297
	OA	1.227	1.227	1.350	1.350
	Or		1.227		
	H				
third-neighbor LJ <sup>c</sup>	type	53A6	56A6 <sub>CARBO</sub> <sup>d</sup>	53A6 <sub>OXY</sub>	53A6 <sub>OXY+D</sub>
$C_6^{1/2}$ (kJ mol <sup>-1</sup> nm <sup>12</sup> ) <sup>1/2</sup>	CH2	0.06873	0.06873	0.06873	0.06873
	CH2r	0.06873	0.06873	0.06873	0.06873
	CH3	0.08278	0.08278	0.08278	0.08278
	OE	0.04756	0.04756	0.04756	0.04756
	OA	0.04756	0.04756	0.04756	0.04756
	Or		0.04756		
	H				
$C_{12}^{1/2}$ (10 <sup>-3</sup> [kJ mol <sup>-1</sup> nm <sup>12</sup> ] <sup>1/2</sup> )	CH2	2.178	2.178	2.178	2.178
	CH2r	2.178	1.360	2.178	2.178
	CH3	2.456	2.456	2.456	2.456
	OE	1.125	1.125	1.125	1.125
	OA	1.125	1.125	1.125	1.125
	Or		0.685		
	H				
atomic partial charges $q$ (e)		53A6	56A6 <sub>CARBO</sub>	53A6 <sub>OXY</sub>	53A6 <sub>OXY+D</sub>
ether function: <sup>e</sup>	CHn <sup>f</sup>	0.162	0.232	0.290	0.290
	OE	-0.324	-0.464	-0.580	-0.580
alcohol function:	CHn <sup>f</sup>	0.266	0.232	0.290	0.290
	OA	-0.674	-0.642	-0.700	-0.700
	H	0.408	0.410	0.410	0.410

<sup>a</sup>The parameter sets considered are 53A6<sup>82</sup>, 56A6<sub>CARBO</sub><sup>47</sup>, 53A6<sub>OXY</sub><sup>48</sup>, and 53A6<sub>OXY+D</sub> (this work). Only the parameters relevant for the compounds of Figure 1 are reported. They include the Lennard-Jones (LJ) dispersion parameter  $C_6^{1/2}$ , repulsion parameter for non-hydrogen-bonding interactions  $C_{12,I}^{1/2}$ , and repulsion parameter for hydrogen-bonding interactions  $C_{12,II}^{1/2}$ , for either normal or third-neighbor interactions, as well as the atomic partial charges  $q$ . The functional forms of the corresponding terms and the applied (geometric-mean) combination rule for LJ parameters are described in refs 39 and 41. The parameters of 56A6<sub>CARBO</sub>, 53A6<sub>OXY</sub>, and 53A6<sub>OXY+D</sub> that differ from 53A6 are shown in italics. <sup>b</sup>There is no  $C_{12,III}^{1/2}$  (charged-hydrogen-bonding interactions) for the atom type listed here. <sup>c</sup>There is only one type of  $C_{12}^{1/2}$  parameter for third-neighbors in GROMOS. <sup>d</sup>In 56A6<sub>CARBO</sub> there also exists additional rules (LJ exceptions) for third- and fourth-neighbors in six-membered ring systems (see Table 5 in ref 47, irrelevant here). <sup>e</sup>For 56A6<sub>CARBO</sub>, the indicated atom types refer to an ether in a chain (different types are used for six-membered ring systems). <sup>f</sup>C, CH1, CH2, or CH3, depending on the substitution.

The (average) radius of gyration  $R_g$  is calculated as

$$R_g = \left( \left\langle \left( \sum_i m_i \right)^{-1/2} \left( \sum_i m_i d_i^2 \right)^{1/2} \right\rangle \right) \quad (1)$$

where  $m_i$  is the mass of atom  $i$  and  $d_i$  is its distance from the center of mass of the molecule, while  $\langle \dots \rangle$  stands for ensemble (trajectory) averaging. In polymer theory,<sup>22</sup> one typically expects as a first approximation that the dependence of  $R_g$  on

the molecular weight  $M_w$  of the polymer will obey a power-law of the form

$$R_g = a_g M_w^{\nu_g} \quad (2)$$

where  $a_g$  (offset) and  $\nu_g$  (size or Flory exponent) are constants depending on the polymer type and on the experimental conditions (nature of the solvent, temperature, concentration). For a nonself-avoiding random-walk,  $\nu_g$  can be calculated



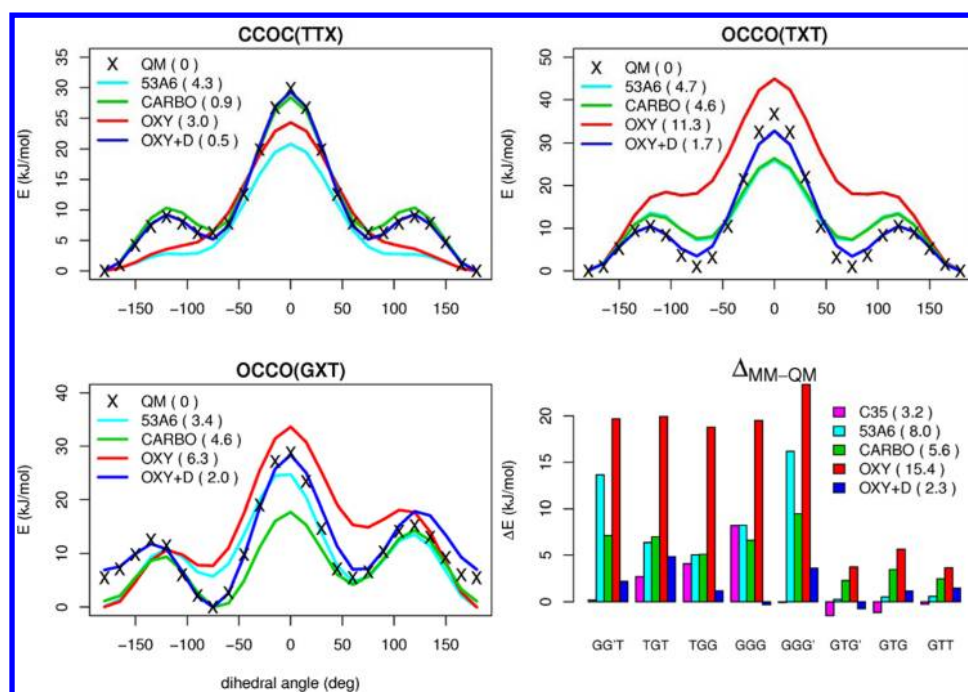


**Figure 2.** Relative potential energies of different conformations of 1,2-dimethoxyethane (DXE) in vacuum. The top and bottom left panels represent potential-energy profiles corresponding to rotations around the different dihedral angles. The configurations considered here are TXT or GXT for OCCO, and TTX for CCOC, where X is the dihedral angle under consideration and the two other dihedral angles are constrained to a fixed value, corresponding to *gauche plus* (G, 60°) or *trans* (T, 180°) conformations. The crosses (x) indicate QM results at the MP2/cc-pVTZ/MP2/6-31G(d) level of theory, taken from ref 27. The lines correspond to results obtained using different GROMOS parameter sets, namely 53A6 (ref 82, cyan), 56A6<sub>CARBO</sub> (ref 47, green), 53A6<sub>OXY</sub> (ref 48, red), and 53A6<sub>OXY+D</sub> (this work, blue). All curves for the potential energy  $E$  correspond to relaxed structures and are anchored to a value of zero at the location of their global minimum. The root-mean-square deviation relative to the QM profile is indicated in the legend, in units of kJ mol<sup>-1</sup>. Note that the cyan curve is almost eclipsed by the green curve in the top right panel. The bottom right panel compares the potential energies of the different low-energy conformers (Table 3, except G'GG') relative to TTT in the four GROMOS force-field versions and in the CHARMM C35 force field<sup>27</sup> with the corresponding relative energies at the QM level (taken from ref 27), that is, each bar represents  $\Delta E(\text{conformer}) = (E_{\text{MM}}(\text{conformer}) - E_{\text{MM}}(\text{TTT})) - (E_{\text{QM}}(\text{conformer}) - E_{\text{QM}}(\text{TTT}))$ . The corresponding root-mean-square deviation is also indicated in the legend, in units of kJ mol<sup>-1</sup>.

analytically<sup>22</sup> and takes a value of 0.5. For a real polymer in solution, excluded-volume and solvation effects become important. For a polymer in a “good solvent”, that is, when solute–solvent interactions entirely dominate solute–solute interactions,  $\nu_g$  can also be calculated analytically<sup>22,111</sup> and takes a value of  $3/5$  (0.6). This situation is expected to represent a good approximation for diluted polyethers in water at room temperature.<sup>112</sup> In practice, the value of  $\nu_g$  is calculated from the simulations based on (average) values of  $R_g$  corresponding to different  $M_w$ , as the slope of a least-squares-fit line to the graph of  $\ln R_g$  against  $\ln M_w$ .

The (average) persistence length  $L_p$  is calculated based on the (average) bond–vector autocorrelation function

$$C_{b,n} = (N - n)^{-1} \sum_{i=1}^N \sum_{j=1}^N \delta_{i+n,j} \langle \mathbf{u}_i \cdot \mathbf{u}_j \rangle \quad (3)$$

where  $\delta$  is the Kronecker symbol,  $N$  is the number of covalent bonds in the polymer,  $\mathbf{u}_i$  and  $\mathbf{u}_j$  are unit vectors along the  $i^{\text{th}}$  and  $j^{\text{th}}$  bonds ( $\mathbf{u}_i \cdot \mathbf{u}_j$  defining the corresponding bond angle  $\theta_{ij}$ ), and  $n$  (ranging from 0 to  $N - 1$ ) is the bond-order of the correlation, with the particular case  $C_{b,0} = 1$ . In a fully rigid and extended (all-*trans*) polymer,  $C_{b,n}$  evaluates to one for all even values of  $n$ . In polymer theory,<sup>22</sup> one typically expects as a first approximation that the dependence of  $C_{b,n}$  on  $n$  for  $n$  even will follow an exponential decay of the form

$$C_{b,n} = e^{-n_p^{-1}n} \quad (4)$$

where  $n_p$  (persistence number) is a constant depending on the polymer molecule (type and molecular weight) and on the experimental conditions. For a real (semirigid) polymer in solution,  $n_p$  represents an effective measure of the number of bonds after which the polymer direction has been effectively randomized (tangential correlation reduced from 1 to  $e^{-1}$ ), that is, an effective measure of the polymer rigidity. The persistence number  $n_p$  is usually rather expressed as a persistence length  $L_p$  defined as

$$L_p = b_p n_p \quad (5)$$

where  $b_p$  is the covalent bond length. In a “good solvent” situation, the persistence length is expected to be essentially independent of the polymer length. In practice, the value of  $n_p$  is calculated from the simulations based on the (average) functions  $C_{b,n}$  for  $n$  even, as the intercept of a least-squares-fit line to the graph of  $\ln C_{b,n}$  against  $n$  with a horizontal line at  $-1$ . The corresponding value of  $L_p$  is then obtained using  $b_p = 0.148$  nm, that is, the mean between the C–O (0.143 nm) and C–C (0.153 nm) reference bond lengths in the 53A6<sub>OXY+D</sub> parameter set (Table 5).

The rotational autocorrelation function  $C_r(t)$  is calculated as

$$C_r(t) = \langle \langle \mathbf{R}(\tau) \cdot \mathbf{R}(\tau + t) \rangle \rangle \quad (6)$$

Table 6. Conformational Populations of 1,2-Dimethoxyethane (DXE) in the Pure Liquid and in Two Aqueous Mixtures<sup>a</sup>

X <sub>DXE</sub>	state	exp.	C35	C35r	53A6	56A6 <sub>CARBO</sub>	53A6 <sub>OXY</sub>	53A6 <sub>OXY+D</sub>
1.0	TTT	0.120	0.195	0.141	0.367	0.345	0.543	0.045
	TGT	0.395	0.341	0.392	0.101	0.274	0.016	0.320
	TGG'	0.340	0.268	0.283	0.059	0.117	0.016	0.267
	TTG	0.050	0.111	0.081	0.332	0.140	0.358	0.041
	TGG	0.095	0.085	0.103	0.045	0.087	0.005	0.210
	GTG				0.033	0.006	0.024	0.004
	GTG'				0.041	0.007	0.035	0.005
	GGG				0.006	0.009	0.000	0.041
	G'GG'				0.004	0.002	0.001	0.006
	GGG'				0.011	0.012	0.002	0.061
0.6	rmsd	0.000	0.059	0.031	0.248	0.157	0.326	0.077
	TTT	0.090	0.153	0.107	0.357	0.311	0.517	0.034
	TGT	0.480	0.434	0.477	0.110	0.312	0.025	0.353
	TGG'	0.260	0.220	0.230	0.060	0.113	0.018	0.230
	TTG	0.045	0.086	0.063	0.326	0.129	0.363	0.031
	TGG	0.125	0.107	0.123	0.050	0.099	0.009	0.238
	GTG				0.034	0.006	0.027	0.003
	GTG'				0.040	0.007	0.036	0.004
	GGG				0.007	0.009	0.001	0.045
	G'GG'				0.004	0.002	0.001	0.005
0.3	GGG'				0.012	0.012	0.003	0.056
	rmsd	0.000	0.044	0.017	0.258	0.146	0.335	0.081
	TTT	0.050	0.110	0.074	0.348	0.283	0.493	0.023
	TGT	0.550	0.520	0.564	0.118	0.344	0.036	0.394
	TGG'	0.205	0.173	0.172	0.061	0.109	0.022	0.190
	TTG	0.040	0.067	0.045	0.322	0.120	0.363	0.023
	TGG	0.155	0.130	0.145	0.054	0.109	0.014	0.263
	GTG				0.034	0.006	0.030	0.002
	GTG'				0.040	0.006	0.036	0.003
	GGG				0.007	0.010	0.001	0.049
	G'GG'				0.004	0.002	0.002	0.005
	GGG'				0.012	0.011	0.004	0.049
	rmsd	0.000	0.037	0.020	0.278	0.151	0.352	0.086
	rmsd	0.000	0.048	0.023	0.262	0.151	0.338	0.082
	all	0.000	0.048	0.023	0.262	0.151	0.338	0.082

<sup>a</sup>The conformational states refer to the 10 energetically distinct classes of conformers defined in Table 3. The considered mole fractions X<sub>DXE</sub> of DXE in the mixture are 1.0 (pure liquid), 0.6, and 0.3. The experimental data (exp.) corresponds to populations inferred based on Raman spectroscopy at 1 bar and 318 K, taken from ref 91. The other columns correspond to values calculated by simulation using the CHARMM C35 (ref 27, values copied from ref 7) and C35r (ref 7, values copied from ref 7) force fields, as well as the different GROMOS parameter sets, namely, 53A6,<sup>82</sup> 56A6<sub>CARBO</sub>,<sup>47</sup> 53A6<sub>OXY</sub>,<sup>48</sup> and 53A6<sub>OXY+D</sub> (this work), at 1 bar and 318 K. For the GROMOS simulations, the assignment of trajectory configurations of the 10 classes of conformers relied on intervals of  $\pm 60^\circ$  around the ideal value for the attribution of each dihedral angle to the G+, T, or G- well, and on the use of Table 3 to group these configurations. For the experimental data and the CHARMM simulations, only 5 main classes to conformers were considered. In both cases, the populations of all classes considered always add up to one. For each mixture, the root-mean-square deviation (rmsd) relative to the populations of the 5 main classes of conformers is also indicated. Corresponding rotational probability distribution profiles are displayed in Figure 3.

where  $\mathbf{R}(t)$  is the end-to-end vector at time  $t$  and  $\langle\langle\ldots\rangle\rangle$  stands for ensemble (trajectory) averaging as well as averaging over all possible time origins  $\tau$ . This function is typically expected to follow an exponential relaxation, that is,

$$C_r(t) = e^{-t/\tau_r} \quad (7)$$

where  $\tau_r$  is the rotational autocorrelation time characterizing the time scale of molecular tumbling, which depends on the polymer molecule (type and molecular weight) and on the experimental conditions. In practice, the value of  $\tau_r$  is calculated from the simulations based on the function  $C_r(t)$ , as the slope of a least-squares-fit line to the graph of  $\ln C_r$  against  $t$ . The rotational autocorrelation time depends on the molecular weight  $M_w$  of the polymer, and was fitted to a power-law dependence similar to that of eq 2, leading to a corresponding exponent  $\nu_r$ .

### III. RESULTS AND DISCUSSION

#### III.1. Parametrization of the Vicinal Diether Function.

The comparison between energy profiles for the OCCO and CCOC dihedral angles of DXE in vacuum, calculated with a QM method<sup>27</sup> or using the 53A6, 56A6<sub>CARBO</sub>, 53A6<sub>OXY</sub> and 53A6<sub>OXY+D</sub> parameter sets, is shown in Figure 2. The configurations considered for these profiles are TXT or GXT for OCCO, and TTX for CCOC, where X is the dihedral angle under consideration. The energies of the different low-energy conformers (Table 3) relative to TTT in the four GROMOS force-field versions and in the CHARMM C35 force field<sup>27</sup> are also compared to the corresponding QM estimates in the bottom right panel.

The 53A6 and 56A6<sub>CARBO</sub> parameter sets are in acceptable, if not excellent, agreement with the QM results. The CCOC profile is well reproduced by 56A6<sub>CARBO</sub>, but the *cis* transition

barriers and the energies of the *gauche* conformers relative to the *trans* one are clearly underestimated in 53A6. For the two force fields, the *gauche* conformations of OCCO in the TXT profile are too high in energy relative to the *trans* one, and the *cis* transition barrier is too low. In the GXT profile, both force fields overestimate the stability of the *trans* conformer relative to the *gauche* ones. The 53A6<sub>CARBO</sub> set reproduces well the energy difference between the two *gauche* conformations but not the height of the *cis* transition barrier, the inverse being true for 53A6. These observations suggest an underestimation of the *gauche*-effect<sup>51,53–63</sup> for vicinal diether functions in the two sets.

For 53A6, the above observations are not surprising considering that the vicinal diether function was never included in the parametrization of this set. For 56A6<sub>CARBO</sub>, however, it should be kept in mind that this set was calibrated primarily in the context of six-membered ring systems. For example, considering 1-methoxymethyl-tetrahydropyran (MMTP; see red curves in Figure 7c,d of ref 47) the *gauche*-effect on the rotational profile of the methoxymethyl group is seen to be well reproduced (note, however, the same underestimation of the *cis* transition barrier). The appearance of discrepancies in Figure 2 are thus likely due to (i) the structural difference between MMTP and DXE, the former involving a CO bond that is part of a six-membered ring and (ii) the presence of two additional torsional-energy terms in 56A6<sub>CARBO</sub> influencing the OCCO rotation in MMTP (types T10 and T11 in Table 6 of ref 47), omitted in the context of DXE because of their specific design for ring systems. The former reason is probably the main one, considering the small force constants of the two extra torsional-energy terms (1 kJ mol<sup>-1</sup>). In summary, although 56A6<sub>CARBO</sub> accounts very well for the rotational properties of the hydroxymethyl group in carbohydrates,<sup>47</sup> including the influence of the *gauche*-effect on these properties, it seems to be less accurate in the context of noncyclic vicinal diethers.

The agreement with the QM results is significantly worse for the 53A6<sub>OXY</sub> parameter set. The CCOC profile is similar to that for 53A6, but it lacks clear minima in the *gauche* conformations, and the *gauche* conformations of OCCO are even higher in energy relative to the *trans* one for both TXT and GXT. The main reason for this deterioration when going from 53A6 to 53A6<sub>OXY</sub> is certainly the increase in the atomic partial charge of the ether oxygen atom (Table 5), favoring the *trans* conformation of OCCO in terms of bond-dipole interactions (oxygen–oxygen repulsion). Although this charge enhancement is required for a more accurate reproduction of the hydration properties of ethers (ref 48 and Section III.2), the increased discrepancy relative to the QM rotational profiles shows that an explicit torsional correction for the *gauche*-effect<sup>51,53–63</sup> is absolutely essential if the 53A6<sub>OXY</sub> parameter set is to account appropriately for the properties of vicinal diethers. Such corrections have already been provided<sup>47,50,52,58,71,72</sup> for previous versions of the force field (37C4, 45A3, or 53A6), as well as for other force fields (Table 1). The corresponding correction for 53A6<sub>OXY</sub> was obtained by a nonlinear least-squares fitting procedure (Section II.2) and resulted in the new torsional-energy parameters of the set 53A6<sub>OXY+D</sub> (Table 4). Owing to this recalibration, 53A6<sub>OXY+D</sub> is in excellent agreement with the QM results, with root-mean-square deviations of 1.7, 2.0, and 0.5 kJ mol<sup>-1</sup> for the OCCO (TXT), OCCO (GXT), and CCOC (TTX) profiles, respectively. The QM energies of the different low-energy conformers (Table 3) relative to TTT are also very well reproduced by the 53A6<sub>OXY+D</sub> parameter set (Figure 2, bottom

right panel), with a rmsd of 2.3 kJ mol<sup>-1</sup>, similar to the corresponding value of 3.2 kJ mol<sup>-1</sup> for the CHARMM C35 force field.<sup>27</sup>

The comparison between conformational populations of DXE in the pure liquid and in two aqueous mixtures, inferred based on Raman spectroscopy<sup>91</sup> or calculated by simulation using the CHARMM C35 (ref 27, values copied from ref 7) and C35r (ref 7, values copied from ref 7) force fields, as well as the different GROMOS parameter sets 53A6, 56A6<sub>CARBO</sub>, 53A6<sub>OXY</sub>, and 53A6<sub>OXY+D</sub>, is shown in Table 6. The experimental and calculated populations are reported for the 10 energetically distinct classes of conformers defined in Table 3. For each mixture, the root-mean-square deviation relative to experiment (rmsd) is also indicated. For the experimental data and the CHARMM simulations, only 5 classes of conformers were considered. In both cases, the populations always add up to one, which implies that the populations of the 5 classes not considered in the latter studies are effectively “lumped” into those of the 5 others. For the 53A6<sub>OXY+D</sub> parameter set, normalized probability distributions corresponding to rotations around the different dihedral angles of DXE in vacuum, in the pure liquid and in the two aqueous mixtures (as well as in an additional system at mole fraction 0.001, mimicking an infinite-dilution situation) are also displayed in Figure 3.

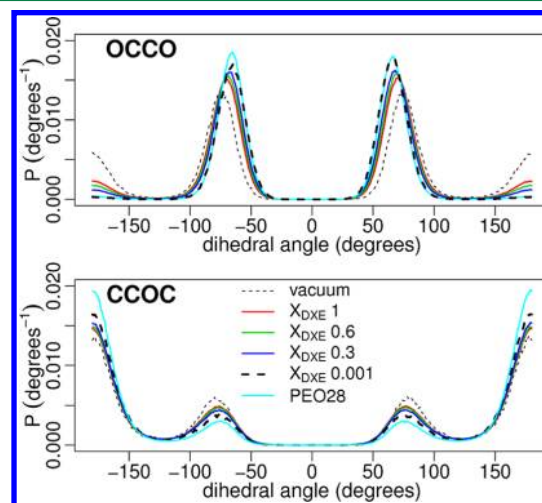


**Figure 3.** Normalized probability distributions corresponding to rotations around different dihedral angles of 1,2-dimethoxyethane (DXE) in different environments and of the corresponding dihedral angles in an aqueous polyethyleneoxide (PEO) oligomer. For DXE, the different distributions correspond to the molecule in vacuum (dashed thin black), in the pure liquid (red), and in three aqueous mixtures (green, blue, and black for DXE mole fractions of  $X_{\text{DXE}}$  of 0.6, 0.3, and 0.001 respectively). The mole fraction of 0.001 corresponds to one DXE molecule in water, and is meant to mimic an infinite-dilution situation. For PEO in aqueous solution (cyan), the oligomer considered encompasses 28 oxygen atoms (PEO28). The corresponding curve for PEG28 (not shown) would be indistinguishable from the PEO28 curve on the scale of the graph. The dihedral angles considered are OCCO (upper panel) and CCOC (lower panel), and the curves are averaged over all occurrences of these dihedral angles in the compound. All the curves correspond to results obtained using the 53A6<sub>OXY+D</sub> parameter set at 1 bar (except DXE in vacuum) and 318 K (DXE) or 296 K (PEO). The probabilities  $P$  are normalized to one. For DXE, conformational populations corresponding to the pure liquid and to the aqueous mixtures with mole fractions 0.6 and 0.3 are reported in Table 6.



Table 7. Thermodynamic Properties of Small Mono- And Diethers<sup>a</sup>

set	compd	$\rho_{\text{liq}}$ (kg m <sup>-3</sup> )	$\Delta H_{\text{vap}}$ (kJ mol <sup>-1</sup> )	$\Delta G_{\text{wat}}$ (kJ mol <sup>-1</sup> )	$\Delta G_{\text{che}}$ (kJ mol <sup>-1</sup> )
exp.	DME	722	21.5	-8.0	
	DEE	708	27.1	-7.4	-12.7
	MPH	736	27.6	-7.0	
	DXE	864	36.4	-20.2	
53A6	DME	750 [1.04]	22.9 (1.4)	1.4 ± 1.0 (9.4)	-9.8 ± 0.8 (-)
	DEE	710 [1.00]	27.7 (0.6)	2.5 ± 1.1 (9.9)	-15.8 ± 1.0 (-3.1)
	MPH	726 [0.99]	29.1 (1.5)	2.1 ± 1.1 (9.1)	-15.4 ± 1.3 (-)
	DXE	855 [0.99]	37.4 (1.0)	-3.5 ± 1.6 (16.7)	-21.1 ± 1.2 (-)
rms		[0.02]	(1.2)	(11.7)	(3.1)
56A6 <sub>CARBO</sub>	DME	776 [1.07]	25.2 (3.7)	-5.9 ± 0.2 (2.1)	-10.6 ± 0.2 (-)
	DEE	723 [1.02]	30.6 (3.5)	-4.3 ± 0.2 (3.1)	-17.6 ± 0.3 (-4.9)
	MPH	740 [1.01]	31.5 (3.9)	-4.8 ± 0.2 (2.2)	-17.5 ± 0.3 (-)
	DXE	882 [1.02]	41.0 (4.6)	-15.0 ± 0.4 (5.2)	-22.2 ± 0.5 (-)
rms		[0.04]	(3.8)	(3.4)	(4.9)
53A6 <sub>OXY</sub> ori	DME	713 [0.99]	24.0 (2.5)	-8.4 ± 1.1 (-0.4)	-7.3 ± 0.9 (-)
	DEE	691 [0.98]	28.0 (0.9)	-6.6 ± 1.6 (0.8)	-13.0 ± 1.4 (-0.3)
	MPH	704 [0.96]	29.3 (1.7)	-6.1 ± 1.5 (0.9)	-13.5 ± 1.2 (-)
	DXE	803 [0.93]	35.7 (-0.7)	-16.1 ± 1.8 (4.1) <sup>b</sup>	-16.9 ± 1.5 (-)
rms		[0.04]	(1.6)	(2.1)	(0.3)
53A6 <sub>OXY</sub> rec	DME	717 [0.99]	23.5 (2.0)	-9.0 ± 0.1 (-1.0)	-7.9 ± 0.2 (-)
	DEE	688 [0.97]	28.5 (1.4)	-7.5 ± 0.3 (-0.1)	-15.1 ± 0.0 (-2.4)
	MPH	702 [0.97]	29.2 (1.6)	-7.9 ± 0.3 (-0.9)	-14.8 ± 0.2 (-)
	DXE	801 [0.93]	35.1 (-1.3)	-14.7 ± 0.1 (5.5)	-16.9 ± 0.7 (-)
rms		[0.03]	(1.6)	(2.8)	(2.4)
53A6 <sub>OXY+D</sub>	DME	717 [0.99]	23.5 (2.0)	-9.0 ± 0.1 (-1.0)	-7.9 ± 0.2 (-)
	DEE	689 [0.97]	28.5 (1.4)	-6.7 ± 0.1 (0.7)	-14.8 ± 0.2 (-2.1)
	MPH	703 [0.96]	29.2 (1.6)	-8.1 ± 0.1 (-1.1)	-15.0 ± 0.3 (-)
	DXE	832 [0.97]	39.6 (3.2)	-21.3 ± 0.1 (-1.1)	-16.4 ± 0.4 (-)
rms		[0.97]	(2.1)	(1.0)	(2.1)

<sup>a</sup>The thermodynamic properties reported are the pure-liquid density  $\rho_{\text{liq}}$  and enthalpy of vaporization  $\Delta H_{\text{vap}}$  at 1 bar and 300 K (except for DME, 254 K), as well as the solvation free energies  $\Delta G_{\text{wat}}$  and  $\Delta G_{\text{che}}$  in water and in cyclohexane at 1 bar and 300 K. The experimental data (exp.) is taken from ref 48 (see references quoted in Table 7 therein). The calculated values correspond to simulations using the GROMOS 53A6,<sup>82</sup> 56A6<sub>CARBO</sub>,<sup>47</sup> 53A6<sub>OXY</sub>,<sup>48</sup> and 53A6<sub>OXY+D</sub> (this work) parameter sets. The results for 53A6 and for 53A6<sub>OXY</sub> labeled "ori" are copied from ref 48. The results for 53A6<sub>OXY</sub> labeled "rec" were recalculated in the present work for consistency checking. The values for  $\Delta G_{\text{wat}}$  and  $\Delta G_{\text{che}}$  correspond to averages over three calculations, the corresponding standard deviation being reported as an error estimate. Values between square brackets represent  $\rho_{\text{liq}}$  ratios (simulation divided by experiment). Values between parentheses represent  $\Delta H_{\text{vap}}$ ,  $\Delta G_{\text{wat}}$  and  $\Delta G_{\text{che}}$  differences (simulation minus experiment). The entries labeled "rms" are the root-mean-square deviations of the above ratios (relative to 1) and differences (simulation relative to experiment), respectively, over the four compounds. <sup>b</sup>The value of -18.5 kJ mol<sup>-1</sup> reported in ref 48 has been mistakenly calculated using slightly different OCCO torsional-energy parameters, whereas that reported (simulation relative to experiment) here (-16.1 kJ mol<sup>-1</sup>) has been recalculated with the exact OCCO torsional-energy parameters for 53A6<sub>OXY</sub> as quoted in Table 4 and the same protocol as in ref 48.

As could be anticipated from the comparison of the rotational profiles for DXE in vacuum against QM data (Figure 2), the 53A6 and 53A6<sub>OXY</sub> parameter sets fail to reproduce the experimental populations, with rmsd values of about 0.25 and 0.33, respectively. In particular, the *trans* OCCO conformers (mainly TTT and TTG) are overrepresented compared to the *gauche* conformers (mainly TGT and TGG'), consequence of an improper representation of the *gauche*-effect. The 56A6<sub>CARBO</sub> set, which provides a somewhat improved description of the QM rotational profiles, suffers to a lesser extent from a similar bias, with rmsd values of about 0.15. In contrast, the 53A6<sub>OXY+D</sub> parameter set leads to populations in excellent agreement with experiment, with rmsd values of about 0.08. The increase of the TGT and TGG populations and decrease of the TTT, TGG' and TTG populations observed experimentally upon increasing the proportion of water in the aqueous mixture are also very well reproduced. Considering Figure 3, these changes correspond to a progressive population shift of the OCCO dihedral angle from *trans* to *gauche*, and of the CCOC dihedral angle from *gauche* to *trans*, upon increasing

the polarity of the environment, from vacuum (permittivity 1) to the pure liquid (permittivity<sup>102</sup> 7.3), and from the pure liquid to mixtures of increasing water contents (permittivities 28.7, 44.9, and 61 for mole fractions 0.6, 0.3, and 0.001 of DXE, respectively, estimated by interpolation using a value<sup>103</sup> of 61 for the SPC water model). The OCCO population shift corresponds to an enhancement of the purely stereoelectronic *gauche*-effect<sup>51,53–63</sup> induced by increased dielectric screening (reduction of the effective electrostatic oxygen–oxygen repulsion), as well as specific hydration effects (water bridging), previously discussed elsewhere.<sup>51,64</sup> The CCOC population shift can also be seen as resulting from increased dielectric screening, which reduces the favorable electrostatic interaction between the positively charged terminal methyl group and their negatively charged fourth-neighbor oxygen atom.

Other DXE models were reported to reproduce the conformer populations extracted from Raman experiments.<sup>7,50,64,77</sup> Among them, both CHARMM versions C35<sup>27</sup> and C35r<sup>7</sup> provide the best agreement with experiment, with rmsd values of about 0.05 and 0.02, respectively. However, five



Table 8. Octanol–Water Partition Coefficient of 1,2-Dimethoxyethane (DXE)<sup>a</sup>

	$\Delta G_{\text{wat}}$ (kJ mol <sup>-1</sup> )	$\Delta G_{\text{oil}}$ (kJ mol <sup>-1</sup> )	$\Delta G_{\text{OW}}$ (kJ mol <sup>-1</sup> ) <sup>b,c</sup>	$\log_{10}(P_{\text{OW}})$
exptl			-1.2	-0.21
53A6 <sub>OXY</sub>	-14.7 ± 0.1	-16.4 ± 0.4	1.7 (2.9)	0.30
53A6 <sub>OXY+D</sub>	-21.3 ± 0.1	-17.4 ± 0.4	-3.9 (-2.7)	-0.68 <sup>d</sup>

<sup>a</sup>The thermodynamic properties reported are the solvation free energies  $\Delta G_{\text{wat}}$  and  $\Delta G_{\text{oil}}$  in water and in octanol at 1 bar and 300 K, and the corresponding transfer free energy  $\Delta G_{\text{OW}}$  (process octanol→water) and partition coefficient  $P_{\text{OW}}$  (ratio octanol/water). The experimental data (exptl) is taken from ref 114. The calculated values correspond to simulations using the GROMOS 53A6<sub>OXY</sub><sup>48</sup> and 53A6<sub>OXY+D</sub> (this work) parameter sets. The standard-state in the two solvents refers to identical concentrations (molarities). The values between parentheses represent  $\Delta G_{\text{OW}}$  differences (simulation minus experiment). Note that the experimental  $\log_{10}(P_{\text{OW}})$  value quoted in ref 116 has the wrong sign.<sup>114</sup> <sup>b</sup>Calculated value obtained from the simulations as  $\Delta G_{\text{OW}} = \Delta G_{\text{wat}} - \Delta G_{\text{oil}}$ . <sup>c</sup>Experimental value calculated from “log(P)” data<sup>114</sup> as  $\Delta G_{\text{OW}} = -\Delta G_{\text{WO}} = \ln(10) RT \log_{10}(P_{\text{OW}})$ . <sup>d</sup>The corresponding value considering hydrated octanol is -0.33 (see text).

classes of conformers (GTG, GTG', GGG, G'GG', and GGG') were not considered in the Raman study as well as in the CHARMM simulations. In the Raman study of ref 91, it is stated that these conformers were not considered, as very low populations rendered their detection difficult. In the CHARMM simulations<sup>7</sup> they were not considered either. However, earlier work on DXE comparing the results of density-functional theory (DFT) calculations with those of Raman and infrared (IR) spectroscopy experiments suggested that the GTG and GGG conformers are actually populated in the liquid state.<sup>113</sup> Based on the present 53A6<sub>OXY+D</sub> results, the populations of the five missing classes add up to about 0.10, and it is not entirely clear how these conformer populations were “lumped” into those of the five classes actually considered (TTT, TGT, TGG', TTG, and TGG) in the Raman and CHARMM studies. Considering these points and the indirect nature of population determinations based on Raman spectra (which also requires specific approximations), a rmsd value below 0.10, as achieved by CHARMM C35 and C35r as well as GROMOS 53A6<sub>OXY+D</sub>, is certainly entirely sufficient, and a further assessment of the relative accuracies of these three sets based on differences below this threshold would not be very meaningful.

**III.2. Thermodynamic Properties of Small Mono- and Diethers.** The thermodynamic properties of the small mono- and diethers DME, DEE, MPH and DXE (Figure 1) as calculated using the 53A6, 56A6<sub>CARBO</sub>, 53A6<sub>OXY</sub>, and 53A6<sub>OXY+D</sub> parameter sets are compared to each other and to experimental data in Table 7. For 53A6<sub>OXY</sub>, two distinct entries labeled “ori” and “rec” correspond to results directly copied from ref 48 and recalculated in the present study, respectively. The slight differences are due to minor alterations in the simulation protocol, including in particular the approach employed for the calculations in vacuum (multiple copies with Berendsen thermostat in ref 48 vs single molecule with stochastic thermostat in the present work).

As discussed previously,<sup>48</sup> the 53A6 parameter set reproduces well the pure-liquid properties  $\rho_{\text{liq}}$  and  $\Delta H_{\text{vap}}$  for ethers, as well as  $\Delta G_{\text{che}}$  for which only one experimental value is available (DEE), but systematically underestimates the magnitude of the hydration free energy. Considering 56A6<sub>CARBO</sub>,  $\rho_{\text{liq}}$  is also well reproduced whereas  $\Delta H_{\text{vap}}$  and the magnitude of  $\Delta G_{\text{che}}$  (DEE) are somewhat overestimated. However, the agreement with experiment in terms of the hydration free energy  $\Delta G_{\text{wat}}$  is greatly improved over 53A6. These changes are related to the charge increase of the ether oxygen atom (from -0.324 to -0.464 *e*), which enhances the polarity of the four molecules. In 53A6<sub>OXY</sub>, this charge is further increased (to -0.580 *e*), along with a readjustment of the Lennard-Jones interaction

parameters for the corresponding atom type OE, which again improves the agreement with experiment in terms of  $\Delta G_{\text{wat}}$ . Compared to 53A6, the root-mean-square deviation (rms) over the four ethers is reduced from 11.7 to 2.1 kJ mol<sup>-1</sup>, without significantly affecting the reproduction of the three other properties.

The 53A6<sub>OXY+D</sub> parameter set provides results similar to the 53A6<sub>OXY</sub> set. The values for the monoether DME are actually rigorously identical, considering that the change does not affect any parameter relevant for this compound. The values for the monoethers DEE and MPH are only affected by the reparametrization of the CCOC dihedral angle (two occurrences in DEE, one in MPH), which only results in a marginal change of the calculated properties. For the diether DXE, the change from 53A6<sub>OXY</sub> to 53A6<sub>OXY+D</sub> increases  $\rho_{\text{liq}}$  and  $\Delta H_{\text{vap}}$ , increases the magnitude of  $\Delta G_{\text{wat}}$  and has essentially no influence on  $\Delta G_{\text{che}}$ . These changes are easily understood considering the different conformational population distributions for DXE in the two force fields (Figure 3 and Table 6). Since 53A6<sub>OXY</sub> underestimates the *gauche*-effect, it overpopulates conformations with the OCCO dihedral angle in the *trans* configuration, both in the pure liquid and in aqueous solution. These conformations present a lower dipole moment compared to the *gauche* conformations (e.g., 0.0 D for TTT vs about 2.8, 2.9, 3.0, or 4.1 D for TGG', TGT, TTG, and TGG, respectively, within 53A6<sub>OXY</sub>), so that intermolecular (pure liquid) and hydration (aqueous solution) interactions are weakened. The observed changes in  $\rho_{\text{liq}}$ ,  $\Delta H_{\text{vap}}$ , and  $\Delta G_{\text{wat}}$  from 53A6<sub>OXY</sub> to 53A6<sub>OXY+D</sub> are thus likely caused by a shift toward *gauche* conformations. Note that since cyclohexane is a nonpolar solvent,  $\Delta G_{\text{che}}$  is considerably less sensitive to the dipole moment of the solute molecule compared to  $\Delta G_{\text{wat}}$ . As a result, for DXE, 53A6<sub>OXY+D</sub> reproduces equally well the experimental  $\rho_{\text{liq}}$  (rms equal to 3%), slightly less well the experimental  $\Delta H_{\text{vap}}$  (rms increased from 1.6 to 2.1 kJ mol<sup>-1</sup>), significantly better the experimental  $\Delta G_{\text{wat}}$  (rms reduced from 2.8 to 1.0 kJ mol<sup>-1</sup>), while  $\Delta G_{\text{che}}$  remains unchanged (calculated value from -16.9 to -16.4 kJ mol<sup>-1</sup>). The above comparison between 53A6<sub>OXY</sub> and 53A6<sub>OXY+D</sub> underlines that agreement with experimental thermodynamic data is a necessary but not a sufficient condition for the accuracy of a force field. Such an agreement is achieved to comparable extents by the two force fields (except maybe for the larger  $\Delta G_{\text{wat}}$  deviation in 53A6<sub>OXY</sub>), but 53A6<sub>OXY</sub> performs quite poorly in terms of the conformational distribution of DXE.

Due to its particular chemical composition, DXE is a compound that presents a comparable affinity for both polar and nonpolar solvents.<sup>6</sup> Combined together, the results for  $\Delta G_{\text{wat}}$  and  $\Delta G_{\text{che}}$  in 53A6<sub>OXY+D</sub> suggest a somewhat higher

affinity of DXE for water compared to cyclohexane, while  $53A6_{\text{OXY}}$  suggests the opposite trend. Octanol–water transfer free energies  $\Delta G_{\text{OW}}$  (process octanol→water) and partition coefficients  $P_{\text{OW}}$  (ratio octanol/water) for DXE as calculated using the  $53A6_{\text{OXY}}$  and  $53A6_{\text{OXY+D}}$  parameter sets are compared to experimental data<sup>114</sup> in Table 8. The  $53A6_{\text{OXY}}$  parameter set leads to a positive  $\Delta G_{\text{OW}}$  value of 1.7 kJ mol<sup>−1</sup>, resulting in a  $\log_{10}(P_{\text{OW}})$  estimate of 0.30, which suggests a higher affinity of DXE for octanol compared to water. In contrast, the  $53A6_{\text{OXY+D}}$  parameter set leads to a negative  $\Delta G_{\text{OW}}$  value of −3.9 kJ mol<sup>−1</sup>, resulting in a  $\log_{10}(P_{\text{OW}})$  estimate of −0.68, which suggests in the opposite a higher affinity for water compared to octanol. Experimentally, the latter trend is correct, with a measured  $\log_{10}(P_{\text{OW}})$  value of −0.21. As previously discussed in the context of the  $\Delta G_{\text{wat}}$  and  $\Delta G_{\text{che}}$ , the conformational population shift from  $53A6_{\text{OXY}}$  to  $53A6_{\text{OXY+D}}$  favors more polar species. This has a limited effect on the solvation free energy  $\Delta G_{\text{otl}}$  in the relatively nonpolar solvent octanol, but it largely increases the magnitude of the hydration free energy  $\Delta G_{\text{wat}}$ , tipping the balance toward water in terms of solvent affinity. Although the error between calculated and experimental  $\Delta G_{\text{OW}}$  values is of comparable magnitude for both parameter sets (about 2.8 kJ mol<sup>−1</sup>, positive for  $53A6_{\text{OXY}}$  and negative for  $53A6_{\text{OXY+D}}$ ), only  $53A6_{\text{OXY+D}}$  predicts the correct trend of a preferential affinity for water compared to octanol. Furthermore, it should be recalled that, in an experimental set-up, octanol is typically significantly hydrated (about 0.2 to 0.3 mol fraction water in the octanol phase at saturation<sup>115</sup>). As a result, if DXE intrinsically presents a higher affinity for water compared to octanol, as predicted by the present calculations with  $53A6_{\text{OXY+D}}$  and supported by experiment, it is expected that the calculated transfer free energy (pure octanol to water) should be more negative than its experimental counterpart (water-saturated octanol to water). This hypothesis was subsequently confirmed by a corresponding free-energy calculation considering hydrated octanol (water mole fraction 0.16) as a solvent (Niels Hansen, to be published), resulting in a  $\log_{10}(P_{\text{OW}})$  value  $-0.33 \pm 0.23$ , in much better agreement with the experiment value<sup>114</sup> of −0.21.

Other models of DXE have been shown to reproduce well the density, heat of vaporization and hydration free energy.<sup>27,50</sup> In the recently developed model of Roccatano and co-workers,<sup>50</sup> the calculated  $\log_{10}(P_{\text{OW}})$  for (dry) octanol is reported to be 0.28.<sup>116</sup> This number suggests a higher affinity of DXE for octanol compared to water, whereas the  $53A6_{\text{OXY+D}}$  model presents the opposite trend. Note that the experimental value quoted in ref 116 has the wrong sign,<sup>114</sup> incorrectly suggesting that the trend reported in this study is the one compatible with experiment.

**III.3. Polyether Simulations.** The results of the polyether simulations using the  $53A6_{\text{OXY+D}}$  parameter set are shown in Figures 4–9. The oligomers considered in these simulations are PEO10, PEO19, PEO28, PEO37, and PEG28. These simulations were performed using RF electrostatics, except for a single simulation of PEO28 relying on LS (i.e., PME) electrostatics. Three independent 300 ns simulations were carried out for each oligomer considered, except for PEO28, for which six simulations with RF and one with LS were performed, resulting in a total of 19 simulations.

The convergence properties of the time-averaged radius of gyration  $R_g$  for all simulations are illustrated in Figure 4. The convergence of  $R_g$  is very slow in general and, as expected, becomes slower with increasing chain length. As a result, the

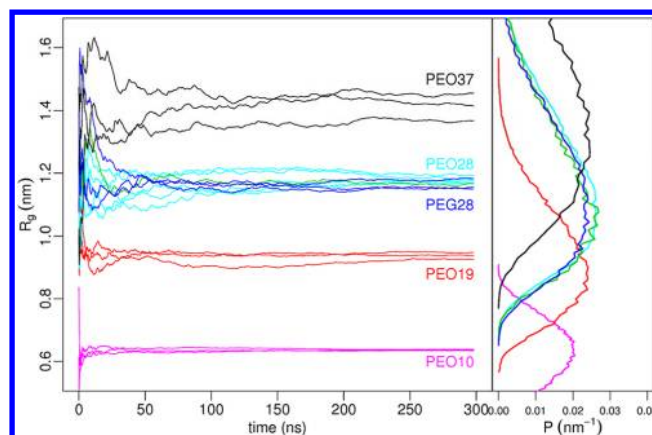


**Figure 4.** Cumulative average of the radius of gyration ( $R_g$ ) as a function of time (left panel) during simulations of polyethylenoxide (PEO) and polyethyleneglycol (PEG) oligomers of different sizes, along with the corresponding normalized probability distributions  $P$  (right panel). The oligomers considered are PEO10 (magenta), PEO19 (red), PEO28 (cyan and green), PEO37 (black), and PEG28 (blue), where the number indicates the degree of polymerization (number of oxygen atoms in the compound). The curves corresponding to three (six for PEO28) independent simulations are shown for each oligomer considered, all carried out using reaction-field (RF) electrostatics. For PEO28, an additional curve (green) corresponds to a single simulation carried out with lattice-sum (LS, i.e., PME) electrostatics instead. All the curves correspond to results obtained using the  $53A6_{\text{OXY+D}}$  parameter set at 1 bar and 296 K. The final average values of  $R_g$  are displayed in Figure 5 as a function of the molecular weight. The numerical results (mean and standard deviation) over all simulations of a given system are  $0.637 \pm 0.002$  (PEO10),  $0.94 \pm 0.01$  (PEO19),  $1.17 \pm 0.01$  (PEO28 with RF),  $1.17$  (PEO28 with LS),  $1.16 \pm 0.02$  (PEG28), and  $1.41 \pm 0.04$  (PEO37) nm.

final averages are affected by larger uncertainties for the longest oligomers considered.

These average values of  $R_g$  are displayed in Figure 5 as a function of the molecular weight  $M_w$ , on a double-logarithmic scale. In line with the slower convergence properties upon increasing the chain length, the spread in the values calculated for the three (six) independent simulations for each oligomer increases with  $M_w$ . The incurred error remains nevertheless acceptable, considering that for the largest oligomer, PEO37, the maximal difference between the three calculated  $R_g$  values is 0.1 nm over an average of about 1.4 nm. The inset of Figure 5 also shows that the use of LS instead of RF electrostatics for PEO28 has no statistically significant influence on  $R_g$ , and that PEG28 behaves very similarly to PEO28 in terms of  $R_g$ , taking into account that its molecular weight is slightly lower, resulting in a slightly lower  $R_g$ . The probability distributions of the OCCO and CCOC dihedral angles were also monitored for PEO28 and PEG28. The curves for PEO28 are shown in Figure 3. The corresponding curves for PEG28 (not shown) are entirely indistinguishable from these on the scale of the graph. The absence of a significant difference between PEO and PEG in the limit of long chains, already observed here for PEO28 and PEG28, is expected considering that the two types of polymers only differ in structure at the level of their termini (Figure 1). The same observation was made previously in simulations employing the CHARMM C35r force field.<sup>7</sup> Following from these considerations, the rest of the discussion

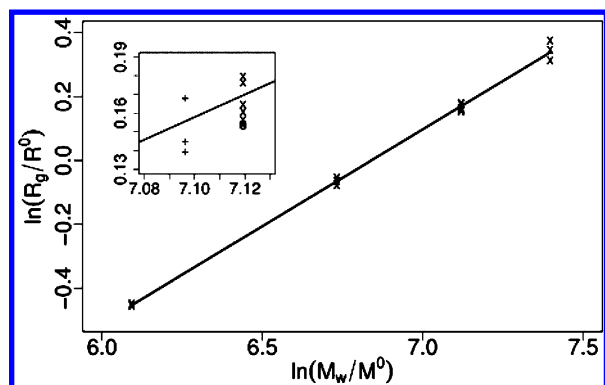


**Figure 5.** Average radius of gyration ( $R_g$ ) calculated from simulations of polyethyleneoxide (PEO) and polyethyleneglycol (PEG) oligomers of different sizes, displayed as a function of the molecular weight ( $M_w$ ) on a double-logarithmic scale. The oligomers considered are PEO10, PEO19, PEO28, PEO37, and PEG28, where the number indicates the degree of polymerization (number of oxygen atoms in the compound). The points corresponding to three (six for PEO28) independent simulations are shown for each oligomer considered, all carried out using reaction-field (RF) electrostatics. For PEO28, an additional point corresponds to a single simulation carried out with lattice-sum (LS, i.e., PME) electrostatics instead. The crosses (x) correspond to PEO simulations using RF. The plus (+) and circle (o) symbols (inset only) correspond to the PEG28 simulations and to the PEO28 simulation using LS, respectively. The double-logarithmic scale is defined by natural logarithms (ln) with the reference units  $M^0 = 1 \text{ g mol}^{-1}$  and  $R^0 = 1 \text{ nm}$ . The straight line represents a least-squares fit to the data (PEO only), see eq 2, and has an intercept  $a_g = 0.015 \text{ nm}$  and a slope  $\nu_g = 0.61$ . All the points correspond to results obtained from 300 ns simulations using the 53A6<sub>OXY+D</sub> parameter set at 1 bar and 296 K. The corresponding cumulative averages of  $R_g$  are displayed in Figure 4 as a function of time.

will exclusively focus on the properties of the PEO oligomers based on the RF simulations.

As expected from eq 2 for a polymer in a “good solvent”, that is, when solute–solvent interactions entirely dominate solute–solute interactions, the (average) radius of gyration  $R_g$  (Figure 5, main graph) follows a straight line as a function of the molecular weight  $M_w$  when displayed on a double-logarithmic scale, with an offset  $a_g = 0.015 \text{ nm}$  and a slope (size exponent)  $\nu_g = 0.61$  nearly equal to  $3/5$  (0.6). Experimentally, the size exponent for PEO has been evaluated using photon correlation spectroscopy,<sup>117</sup> resulting in  $\nu_g = 0.565 \pm 0.018$ , and by light scattering experiments,<sup>118</sup> resulting in  $\nu_g = 0.583 \pm 0.031$ . It is important to stress, however, that these experiments concerned much longer polymer chains, with molecular weights on the order of 100–1000 kDa (i.e., 1–3 orders of magnitude longer). The size exponent was also evaluated using other computational models of PEO. Estimates of 0.528 and 0.515 were reported using the CHARMM C35<sup>27</sup> and C35r<sup>7</sup> force fields, respectively (based on a weighted linear least-squares fit). Using their reoptimized version of the GROMOS 45A3 force field, Larson and co-workers<sup>52</sup> reported values of 0.549 and 0.576 for two different box sizes. Using TraPPE-UA with modified torsions from Anderson and Wilson,<sup>74,75</sup> Sadowski and co-workers<sup>77</sup> arrived at a significantly higher exponent of 0.752 (note that our own fitting of the raw data provided in ref 77 leads to a value of 0.698 instead). However, the latter study considered simulated systems encompassing multiple (eight or more) PEO molecules in the computational box. It is also worth mentioning that theoretical arguments have been put

forward to rationalize either positive (short chain oligomers tend to be stiffer<sup>77</sup>) or negative (reduction of excluded-volume effects for short oligomer chains<sup>7</sup>) deviations from the ideal value of 0.6 in the context of short oligomers.

The distributions of the persistence length  $L_p$  calculated from the different PEO28 simulations based on eqs 3–5 are shown in Figure 6. The corresponding curves for the other PEO

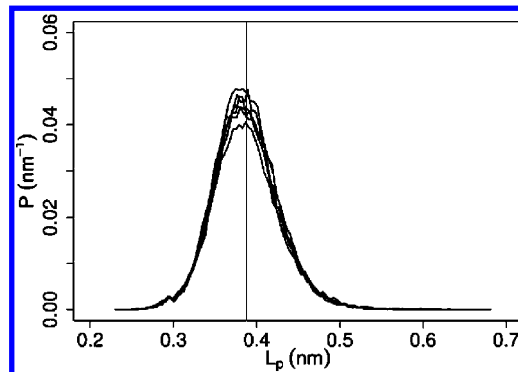


**Figure 6.** Normalized probability distributions of the persistence length ( $L_p$ ) calculated from simulations of a polyethyleneoxide (PEO) oligomer. The PEO oligomer considered encompasses 28 oxygen atoms (PEO28). The curves correspond to six independent simulations, all carried out using reaction-field (RF) electrostatics. Corresponding curves calculated for the other oligomers considered (PEO10, PEO19, PEO28, PEO37, and PEG28) are essentially identical (not shown). The curves correspond to results obtained from 300 ns simulations using the 53A6<sub>OXY+D</sub> parameter set at 1 bar and 296 K. The vertical line indicates the average over the six trajectories,  $L_p = 0.39 \pm 0.04 \text{ nm}$  (mean, standard deviation).

oligomers (not shown) are very similar to these on the scale of the graph, matching the expectation that, in a “good solvent” situation, the persistence length is a characteristic constant of the polymer type and is essentially independent of the polymer length. For all PEO oligomers, the (average) value  $L_p$  calculated based on the simulations is  $0.39 \pm 0.04 \text{ nm}$ , a corresponding estimate for PEG based on the PEG28 simulations being  $0.37 \pm 0.01 \text{ nm}$ , very similar to PEO28. Experimentally, the persistence length of PEO has been evaluated from force temperature measurements,<sup>119</sup> interpreted using the rotational isomeric state (RIS) model, resulting in  $L_p = 0.37 \text{ nm}$ . Another estimate of  $L_p = 0.98 \text{ nm}$  was also reported,<sup>120</sup> but it concerned PEO in a saline solution (0.45 M  $\text{K}_2\text{SO}_4$ ) and was evaluated at the  $\theta$ -temperature<sup>22,121</sup> of the polymer (about 34.5 °C; under these conditions the polymer shape follows a random-walk and  $\nu$  reduces to 0.5). More recently, a determination based on atomic force microscopy<sup>122</sup> resulted in  $L_p = 0.41 \text{ nm}$ . Finally, based on simulations using the CHARMM force field, fitted using the worm-like chain model,<sup>22</sup> values of  $0.43 \pm 0.03 \text{ nm}$  and  $0.37 \pm 0.04 \text{ nm}$  were derived for the C35 and C35r parameter sets, respectively.<sup>7</sup>

The rotational autocorrelation functions  $C_r(t)$  of the end-to-end vector calculated using eq 6 for the different PEO simulations are shown in Figure 7. Based on a fit to eq 7, the corresponding rotational correlation times  $\tau_r$  are estimated to be about 0.31 (PEO10), 0.89 (PEO19), 1.6 (PEO28), and 3.0 (PEO37) ns. As shown in the inset of Figure 7, these characteristic times increase with the molecular weight, following a power law similar to that observed for the radius of gyration, with an exponent  $\nu_r = 1.7$ . This value is very similar to that found by Sadowski and co-workers ( $\nu_r = 1.8$ , although



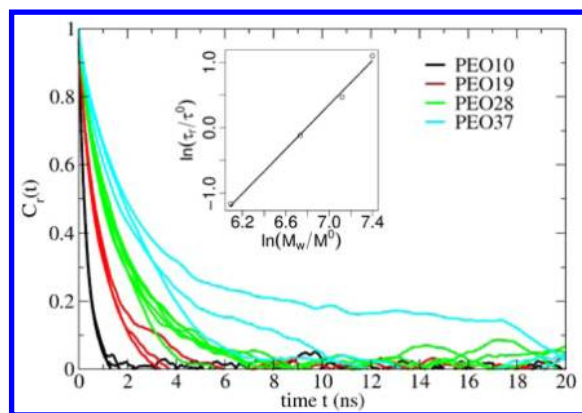


**Figure 7.** Rotational autocorrelation functions ( $C_r(t)$ ) calculated from simulations of polyethyleneoxide (PEO) oligomers of different sizes, and corresponding characteristic time ( $\tau_r$ ) displayed as a function of the molecular weight ( $M_w$ ) on a double-logarithmic scale (inset). The oligomers considered are PEO10, PEO19, PEO28, and PEO37, where the number indicates the degree of polymerization (number of oxygen atoms in the compound). The curves corresponding to three (six for PEO28) independent simulations are shown for each oligomer considered, all carried out using reaction-field (RF) electrostatics. Fitting the curves to a single exponential leads to characteristic times  $\tau_r$  of  $0.312 \pm 0.006$  ns (PEO10),  $0.89 \pm 0.08$  ns (PEO19),  $1.6 \pm 0.1$  ns (PEO28), and  $3.0 \pm 0.9$  ns (PEO37). In the inset, the double-logarithmic scale is defined by natural logarithms ( $\ln$ ) with the reference units  $M^0 = 1$  g mol $^{-1}$  and  $\tau^0 = 1$  ns. The straight line represents a least-squares fit to the data and has an intercept  $a_r = 0.01 \times 10^{-3}$  ns and a slope  $\nu_r = 1.70$ . All the points correspond to results obtained from 300 ns simulations using the 53A6<sub>OXY+D</sub> parameter set at 1 bar and 296 K.

with a different force field and considering multiple copies of the oligomers). A power-law dependence is in line with the behavior expected for a polymer in a “good solvent”.<sup>123,124</sup>

Considering the probability distributions of the OCCO and CCOC dihedral angles for PEO28 (Figure 3), the trends observed in the context of DXE (Section III.1) upon increasing environment polarity (enhancement of the *gauche* OCCO and *trans* CCOC populations), from vacuum to the pure liquid and to increasingly dilute aqueous solutions, appear to further continue when considering PEO oligomers. This finding may appear somewhat counterintuitive at first sight. For example, in the context of proteins, the local environment of a functional group within the folded polymer (native state) is expected to be of much lower polarity compared to a pure water environment. Figure 3 suggests, however, that this argument does not apply in the context PEO. Rather, it seems that the partially folded polymer environment represents for the PEO diether functions a medium with about the same (or even a slightly higher) effective polarity compared to pure water.

As an attempt to rationalize this surprising observation, the local oxygen atom number densities  $\eta(r)$  as a function of the distance  $r$  from the ether oxygen atoms (OE) of DXE or PEO were monitored for all these systems, as well as the PEO10 and PEO37 systems, considering separately as neighbors either water oxygen atoms (OW) or other ether oxygen atoms (OE'). Note that the function  $\eta(r)$  corresponds to an OE-centered radial distribution function amplified by the bulk atom number density of the considered neighbor atoms (OW or OE'), and that the integral of  $4\pi r^2 \eta(r)$  up to a certain distance corresponds to the total number of neighbor atoms of this

type within the corresponding distance range. The results of this analysis are shown in Figure 8.

For DXE at infinite dilution, the diether function appears to “adsorb” a number of water molecules corresponding to first-shell hydrogen-bonded saturation of its oxygen atoms, with an average first-shell coordination number of 1.9 OW atoms per OE atom. This number slightly decreases to 1.8 for PEO10 and 1.7 for PEO28, but does not seem to decrease further when the polymer size increases (a value of 1.7 is also found for PEO37, not shown in Figure 8). This can be explained by the higher number of neighboring OE atoms when the oligomer size increases, which slightly compete for OW atoms in the first shell. However, the difference is so small that longer PEO oligomers can be considered to have their OE saturated just as one DXE molecule (which is in fact PEO2). For the aqueous mixtures at DXE mole fractions 0.6 and 0.3, this saturation level is not reached, the corresponding coordination numbers being about 0.4 and 0.9, respectively. For  $X_{\text{DXE}} = 0.3$ , this coordination number is above the average OW-to-OE ratio for this system (i.e., 0.33), suggesting that most of the water molecules in this simulation are “trapped” in the first coordination shell of at least one OE atom. However, it does not apply for the system at  $X_{\text{DXE}} = 0.6$ , for which the average OW-to-OE ratio (1.16) is higher than the coordination number (0.9). For all systems, there is also a clear tendency for secondary ether oxygen atoms OE' (from other DXE molecules or from other diether functions along a PEO chain) to occupy the second-shell of a primary ether oxygen atom OE, suggesting a significant extent of “water bridging”. Interestingly, the extent of “water-bridging” increases from PEO10 to PEO28 and PEO37, that is, the number of second-shell water molecules clearly decreases at the benefit of the number of second-shell ether atoms (PEO28 and PEO37 are, however, very similar in this respect).

As an illustration for the tight PEO–water interactions, Figure 9 shows three trajectory frames corresponding to extreme and intermediate values of  $R_g$  for the PEO28 oligomer. In the three cases, water molecules are seen to make hydrogen-bonds with the ether oxygen atoms, the occurrences of “water bridging” being also clearly visible in the two most compact conformations. In such compact conformations, water molecules may also be “caged” within the polymer.

#### IV. CONCLUSION

The goal of the present work was to adjust the GROMOS 53A6<sub>OXY</sub> force field into a new version 53A6<sub>OXY+D</sub> including an accurate description of vicinal diethers. The reoptimization was based on the compound DXE and involved a fitting of the relevant torsional-energy parameters against QM rotational energy profiles in vacuum, followed by a validation against experimental conformer populations in the pure liquid and in aqueous solutions. A systematic comparison between the 53A6, 56A6<sub>CARBO</sub>, 53A6<sub>OXY</sub> and 53A6<sub>OXY+D</sub> sets was also performed in terms of above properties, as well as in terms of the thermodynamic pure-liquid and solvation properties of the mono- and diethers DME, DEE, MPH, and DXE. Finally, the 53A6<sub>OXY+D</sub> parameter set was further validated in the context of polyethers, namely, PEO and PEG.

By calibration, 53A6<sub>OXY+D</sub> presents excellent agreement with the QM rotational profiles for the OCCO and CCOC dihedral angles of DXE in vacuum, with root-mean-square deviations of 2 kJ mol $^{-1}$  or less. In comparison, 53A6, 56A6<sub>CARBO</sub>, and, even more pronouncedly, 53A6<sub>OXY</sub> underestimate the magnitude of



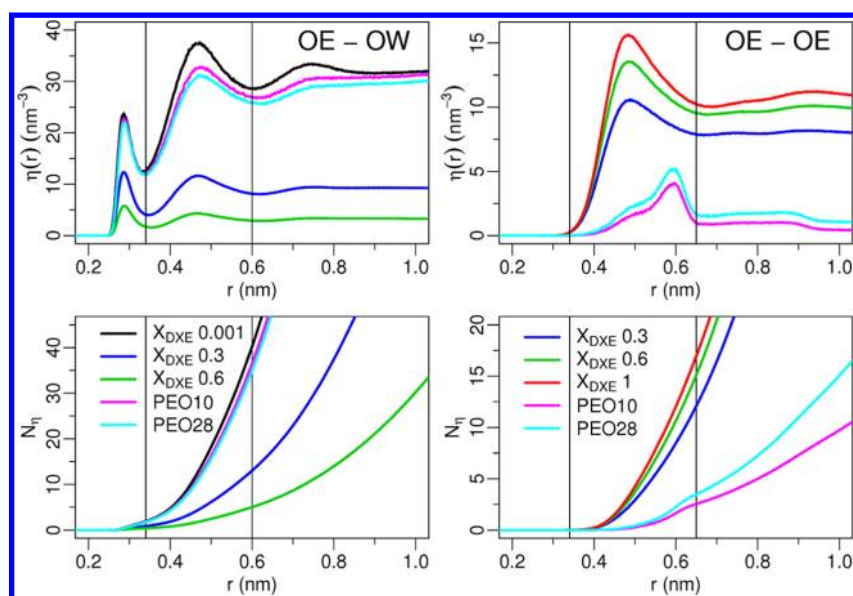


**Figure 8.** Local oxygen atom number densities ( $\eta(r)$ ) as a function of the distance  $r$  from the ether oxygen atoms of 1,2-dimethoxyethane (DXE) in different environments and of aqueous polyethyleneoxide (PEO) oligomers. For DXE, the different functions correspond to the molecule in the pure liquid (red) and in three aqueous mixtures (green, blue, and black for DXE mole fractions  $X_{\text{DXE}}$  of 0.6, 0.3, and 0.001, respectively). The mole fraction of 0.001 corresponds to one DXE molecule in water and is meant to mimic an infinite-dilution situation. For PEO, the oligomers considered are PEO10 (magenta) and PEO28 (cyan), where the number indicates the degree of polymerization (number of oxygen atoms in the compound). For ease of reading, PEO37 has not been represented as the corresponding curves almost overlap with those of PEO28. The function  $\eta(r)$  represents the local number density of neighboring oxygen atoms of a given type in a radial shell of radius  $r$  around a central ether oxygen atom OE, averaged over all possible central oxygen atoms in the system and considering as neighbors either water oxygen atoms OW (top right panel) or other ether oxygen atoms OE' (top left panel). The corresponding running integrals  $N_{\eta}$  of  $4\pi r^2 \eta(r)$  are also displayed (bottom panels). The vertical lines correspond approximately to the limits of the first shell (up to 0.34 nm for OE-OW and 0.65 nm for OE-OE) and second shell (0.34 to 0.6 nm for OE-OW only). The resulting integral for the first shell of OE-OW evaluates to 1.9, 0.9, 0.4, 1.8, and 1.7 OW atoms whereas for the second shell it evaluates to 38.1, 12.1, 4.6, 34.5, and 33.0 for  $X_{\text{DXE}} = 0.001$ ,  $X_{\text{DXE}} = 0.3$ ,  $X_{\text{DXE}} = 0.6$ , PEO10 and PEO28 respectively. For the first shell of OE-OE, the results are 12.0, 15.0, 16.8, 2.5, and 3.5 OE atoms for  $X_{\text{DXE}} = 0.3$ ,  $X_{\text{DXE}} = 0.6$ ,  $X_{\text{DXE}} = 1.0$ , PEO10 and PEO28, respectively. All the curves correspond to results obtained using the S3A6<sub>OXY+D</sub> parameter set at 1 bar and 318 K (DXE) or 296 K (PEO).

the *gauche*-effect, that is, the stereoelectronically induced preference of the OCCO dihedral angle of a vicinal diether for the two *gauche* over the *trans* configuration, although the latter would *a priori* appear to be favored in terms of bond-dipole and steric interactions. The new set also reproduces very well the conformational populations of DXE in the pure liquid and in two aqueous mixtures as inferred from Raman spectroscopy experiments, with a root-mean-square deviation of about 0.08, that is, within the suggested error of about 0.10 for this experimental determination. In particular, the increase in the population of *gauche* over *trans* conformers for the OCCO dihedral angle upon increasing the water content in the mixture and thus, the polarity of the medium, is in line with the experimental observations. It can be interpreted as a consequence of increased dielectric screening, which counteracts the unfavorable bond-dipole interaction and adds a medium-dependent contribution to the purely stereoelectronic *gauche*-effect.

The S3A6<sub>OXY+D</sub> parameter set also reproduces very well the experimental thermodynamic pure-liquid and (polar and nonpolar) solvation properties of small mono- and diethers, with root-mean-square deviations of 3% for  $\rho_{\text{liq}}$ , 2.1 kJ mol<sup>-1</sup> for  $\Delta H_{\text{vap}}$ , 1.0 kJ mol<sup>-1</sup> for  $\Delta G_{\text{wat}}$  and an absolute deviation of 2.1 kJ mol<sup>-1</sup> for  $\Delta G_{\text{che}}$  (available for DEE only) over the four compounds considered. This agreement is, in part, inherited from S3A6<sub>OXY</sub>, which already represented a significant improvement over S3A6 and, to a lesser extent, S6A6<sub>CARBO</sub> in terms of the hydration free energy of ether compounds. Note that, in the context of the diether DXE, the improvement

achieved by S3A6<sub>OXY</sub> was resting on essentially incorrect conformational distributions, underlining that agreement with experimental thermodynamic data is a necessary, but not sufficient, condition for the accuracy of a force field. The refinement of S3A6<sub>OXY</sub> into S3A6<sub>OXY+D</sub>, by increasing the population of higher-dipole *gauche* conformations, led to a decrease in  $\Delta G_{\text{wat}}$  further improving agreement with experiment without significant change in  $\Delta G_{\text{che}}$ . As a result, S3A6<sub>OXY+D</sub> suggests a somewhat higher affinity of DXE for water compared to cyclohexane, while S3A6<sub>OXY</sub> suggested the opposite trend. The same observation holds for octanol–water partition, where S3A6<sub>OXY</sub> and S3A6<sub>OXY+D</sub> lead to calculated transfer free energies  $\Delta G_{\text{OW}}$  (octanol→water) of 1.7 and −3.9 kJ mol<sup>-1</sup>, respectively, to be compared with an experimental estimate of −1.21 kJ mol<sup>-1</sup>. Taking into account the residual hydration of octanol in an experimental setup, rendering it effectively more polar than the pure octanol phase considered in the simulations, S3A6<sub>OXY+D</sub> reproduces correctly the experimental preference, with a deviation occurring in the expected direction. A subsequent calculation with S3A6<sub>OXY+D</sub> considering hydrated octanol indeed led to a value of −1.9 kJ mol<sup>-1</sup>, much closer to experiment.

In the context of aqueous polyethers (considering PEO), the S3A6<sub>OXY+D</sub> parameter set leads to a size exponent  $\nu_g = 0.61$  for the molecular-weight dependence of the radius of gyration, nearly equal to the ideal value of 0.6 for a polymer in a “good solvent”, that is, for which solute–solvent interactions entirely dominate solute–solute interactions. This value is compatible with available experimental data (about 0.57, considering 1–2

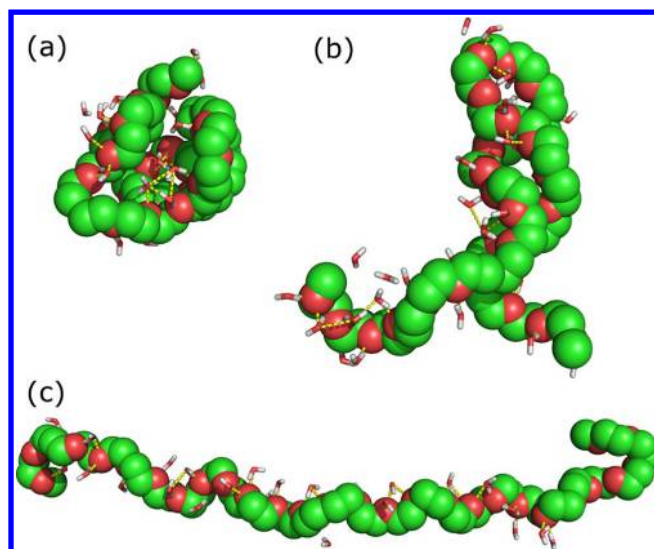


**Figure 9.** Illustrative trajectory frames from the simulations of a polyethyleneoxide (PEO) oligomer in water. The PEO oligomer considered encompasses 28 oxygen atoms (PEO28). The configurations represented correspond to (a) the lowest (0.65 nm), (b) an intermediate (1.41 nm), and (c) the highest (2.17 nm) value of the radius of gyration ( $R_g$ ) observed in the simulations. All water molecules presenting at least one atom within a distance of 0.3 nm or less from any atom of the oligomer are also displayed. Oligomer (united) atoms are displayed as beads, water molecules as sticks, and hydrogen bonds (defined according to the DSSP<sup>126</sup> criterion) as dashed sticks connecting the hydrogen and acceptor oxygen atoms (red, oxygen; green, united-atom carbon; hydrogen, white). These snapshots were extracted from the PEO28 simulations using the 53A6<sub>OXY+D</sub> parameter set at 296 K and 1 bar, and rendered using Pymol.<sup>127</sup>

orders of magnitude longer polymers) and previous simulation results (estimates ranging from 0.52 to 0.64 for oligomers of comparable sizes). The calculated persistence length  $L_p = 0.39 \pm 0.04$  nm, independent of the polymer size, also agrees well with experimentally inferred value (0.37 nm) and previous simulation results (estimates ranging from 0.37 to 0.43 nm for oligomers of comparable sizes). The calculated rotational autocorrelation times (molecular tumbling as described by the end-to-end vector) are found to be on the order of the nanosecond for the oligomers considered, and to follow a power-law increase with the molecular weight (exponent  $\nu_r = 1.7$ ), as also suggested by polymer theory for a polymer in a “good solvent”. Note that the results for PEO are directly transposable to PEG, except for the shortest oligomers, considering that the two types of polymers only differ by the nature of their terminal groups.

Interestingly, the *gauche* population of the diether function in polyethers is similar (even somewhat higher) compared to the corresponding population for aqueous DXE at infinite dilution, suggesting that the partially folded PEO polymer environment represents for this function a medium with about the same (or even a slightly higher) effective polarity compared to pure water. This trend appears to result from the “adsorption” by the polymer of an essentially constant number of water molecules corresponding to first-shell hydrogen-bonded saturation of its oxygen atoms, with an average first-shell coordination number of about 1.9 water molecules per ether atom. In addition, there is also a clear tendency for other ether oxygen atoms along the chain to occupy the second-shell of a primary ether oxygen

atom, suggesting a significant extent of intramolecular second-shell contacts *via* “water bridging”.

These observations can be summarized pictorially by describing polyethers as “water sponges”. The *gauche*-preference of the OCCO dihedral angle is promoted by a combination of the (solvent-independent) stereoelectronic *gauche*-effect and the (solvent-dependent) screening of unfavorable bond-dipole interactions by the environment. The *gauche* population is thus sensitive to the local polarity of the medium surrounding the diether function. Except in very concentrated solutions, the availability of water and the high affinity of water molecules for the polymer are such that they guarantee the first-shell hydrogen-bonded saturation of its oxygen atoms by water, and a significant extent of “water bridging” across the polymer. As a result, the local environment of the diether function is highly polar, that is, of the same (or even a slightly higher) effective polarity compared to pure water.

The “water sponge” picture of PEO, which is nicely compatible with that of a polymer in a “good solvent”, contrasts sharply with the “hydrophobic driving force” situation characteristic of typical water-soluble proteins, the latter involving the “expulsion” of water from the polymer core rather than its “adsorption” within the core. The reason for this different behavior is probably the higher intrinsic polarity of PEO along with its inability to function as a hydrogen-bond donor. While the desolvation cost of polar residues in proteins is compensated by favorable electrostatic (predominantly hydrogen-bonding) interactions in the folded state, such interactions are impossible for PEO in the absence of water. As a result, compact polymer shapes are only possible in this case when water is also included within the core, e.g. in the form of “water bridges”. One may speculate about the possible appearance of specific water-mediated secondary-structure elements (e.g., helices or sheets) in PEO (work is in progress to analyze the present simulations in this direction). However, such elements are bound to be relatively short and labile considering the homogeneity of the PEO chain sequence (no side chains) as opposed to the rich alphabet (twenty natural types of side chains) and nature-optimized encoding afforded by protein sequences. Note that an interesting intermediate situation between those of polyethers and proteins is encountered in the context of depso-proteins,<sup>125</sup> that is, proteins in which the residue alphabet is kept unchanged, but the backbone amide function is replaced by an ester function, only able to function as a hydrogen-bond acceptor.

In terms of force-field development, the results presented here provide convincing evidence for the appropriate parametrization of the vicinal diether function within the 53A6<sub>OXY+D</sub> parameter set. This set is fully compatible with the 53A6<sub>OXY</sub> force field (and its subsequent extension to amides,<sup>90</sup> as well as to other nitrogen compounds, sulfur compounds, and aromatic alcohols; work in progress) and the rest of the GROMOS force field for biomolecules (proteins, nucleic acids, lipids, and carbohydrates). This compatibility is particularly important considering the relevance of PEO- or PEG-hosted and of PEGylated biomolecules. The 53A6<sub>CARBO</sub> set was also considered here in view of a subsequent merging of this carbohydrate-specific force field into 53A6<sub>OXY</sub>. In this context, the consideration of cyclic ethers, which were left out in the present work, will also become very important. Further work using the 53A6<sub>OXY+D</sub> force field in the context of C<sub>4</sub>E<sub>j</sub>

polyether surfactants and their interaction with membrane proteins is also in progress.

## AUTHOR INFORMATION

### Corresponding Author

\*Email: patrick.fuchs@univ-paris-diderot.fr.

### Notes

The authors declare no competing financial interest.

## ACKNOWLEDGMENTS

Financial support from the Swiss National Science Foundation (Grants NF 200021-132739 and 200021-138020) is also gratefully acknowledged, as well as Niels Hansen for providing the results of the wet-octanol calculations. P.F.J.F. was supported by CNRS (France) through a "délégation CNRS" at the Laboratoire d'Imagerie Paramétrique (UMR CNRS/Paris 6).

## DEDICATION

This article is dedicated to Wilfred van Gunsteren in the honor of his 65th birthday. The present study originated from an unlikely French–Norwegian–Swiss–Brazilian collaboration, of the kind that were so nicely promoted by Wilfred's open and generous attitude towards short- and long-term visitors, and by the friendly and enthusiastic atmosphere he insufflates into his group.

## REFERENCES

- (1) Pedersen, C. J. *Science* **1988**, *241*, 536–540.
- (2) Pedersen, C. J. *Angew. Chem., Int. Ed.* **1988**, *27*, 1021–1027.
- (3) Kralj, M.; Tušek-Božić, L.; Frkanec, L. *ChemMedChem* **2008**, *3*, 1478–1492.
- (4) Goldfine, H.; Langworthy, T. A. *Trends Biochem. Sci.* **1988**, *13*, 217–221.
- (5) Paltauf, F. *Chem. Phys. Lipids* **1994**, *74*, 101–139.
- (6) Harris, J. M. *Poly(ethylene glycol) Chemistry: Biotechnical and Biomedical Applications*; Plenum Press: New York and London, 1992.
- (7) Lee, H.; Venable, R. M.; MacKerell, A. D.; Pastor, R. W. *Biophys. J.* **2008**, *95*, 1590–1599.
- (8) Harlan, S. L. In *High-Tech Fibrous Materials*; American Chemical Society: Washington, D.C., 1991; Vol. 457, pp 248–259.
- (9) Morck, R.; Reimann, A.; Kringstad Knut, P. In *Lignin*; American Chemical Society: Washington, DC, 1989; Vol. 397, pp 390–401.
- (10) Rothhauser, B.; Kraus, G.; Schmidt, P. C. *Eur. J. Pharm. Biopharm.* **1998**, *46*, 85–94.
- (11) Zeng, Z.; Phillips, B. S.; Xiao, J.-C.; Shreeve, J. M. *Chem. Mater.* **2008**, *20*, 2719–2726.
- (12) Hanemann, T. *Composites, Part A* **2006**, *37*, 2155–2163.
- (13) Seborg, R. M.; Inverarity, R. B. *Science* **1962**, *136*, 649–650.
- (14) Albertsson, P. A. In *Adv. Protein Chem.*; Academic Press: New York London, 1970; Vol. 24, pp 309–341.
- (15) McPherson, A. J. *Cryst. Growth* **1991**, *110*, 1–10.
- (16) Wiencek, J. M. *Annu. Rev. Biomed. Eng.* **1999**, *1*, 505–534.
- (17) Harris, J. M.; Chess, R. B. *Nat. Rev. Drug Discov.* **2003**, *2*, 214–221.
- (18) Garavito, R. M.; Ferguson-Miller, S. J. *Biol. Chem.* **2001**, *276*, 32403–32406.
- (19) Garavito, R. M.; Picot, D. *Methods* **1990**, *1*, 57–69.
- (20) Tanaka, T. *Experimental Methods in Polymer Science: Modern Methods in Polymer Research and Technology*; Academic Press: San Diego, 2000.
- (21) Berne, B. J.; Pecora, R. *Dynamic Light Scattering: With Applications to Chemistry, Biology, and Physics*; Dover Publications: Mineola, NY, 2000.
- (22) Teraoka, I. *Polymer Solutions: An Introduction to Physical Properties*; Wiley: New York, 2002.
- (23) Feller, S. E.; MacKerell, A. D. *J. Phys. Chem. B* **2000**, *104*, 7510–7515.
- (24) Hatcher, E.; Guvench, O.; MacKerell, A. D. *J. Phys. Chem. B* **2009**, *113*, 12466–12476.
- (25) MacKerell, A. D.; Bashford, D.; Bellott, D.; Dunbrack, R. L.; Evanseck, J. D.; Field, M. J.; Fischer, S.; Gao, J.; Guo, H.; Ha, S.; Joseph-McCarthy, D.; Kuchnir, L.; Kucera, K.; Lau, F. T. K.; Mattos, C.; Michnick, S.; Ngo, T.; Nguyen, D. T.; Prodhom, B.; Reiher, W. E.; Roux, B.; Schlenkrich, M.; Smith, J. C.; Stote, R.; Straub, J.; Watanabe, M.; Wiorkiewicz-Kuczera, J.; Yin, D.; Karplus, M. *J. Phys. Chem. B* **1998**, *102*, 3586–3616.
- (26) MacKerell, A. D.; Wiorkiewicz-Kuczera, J.; Karplus, M. *J. Am. Chem. Soc.* **1995**, *117*, 11946–11975.
- (27) Vorobyov, I.; Anisimov, V. M.; Greene, S.; Venable, R. M.; Moser, A.; Pastor, R. W.; MacKerell, A. D. *J. Chem. Theory Comput.* **2007**, *3*, 1120–1133.
- (28) Cornell, W. D.; Cieplak, P.; Bayly, C. I.; Gould, I. R.; Merz, K. M.; Ferguson, D. M.; Spellmeyer, D. C.; Fox, T.; Caldwell, J. W.; Kollman, P. A. *J. Am. Chem. Soc.* **1995**, *117*, 5179–5197.
- (29) Kirschner, K. N.; Yongye, A. B.; Tschampel, S. M.; González-Outeiriño, J.; Daniels, C. R.; Foley, B. L.; Woods, R. J. *J. Comput. Chem.* **2008**, *29*, 622–655.
- (30) Pearlman, D. A.; Case, D. A.; Caldwell, J. W.; Ross, W. S.; Cheatham III, T. E.; DeBolt, S.; Ferguson, D.; Seibel, G.; Kollman, P. *Comput. Phys. Commun.* **1995**, *91*, 1–41.
- (31) Weiner, P. K.; Kollman, P. A. *J. Comput. Chem.* **1981**, *2*, 287–303.
- (32) Damm, W.; Frontera, A.; Tirado-Rives, J.; Jorgensen, W. L. *J. Comput. Chem.* **1997**, *18*, 1955–1970.
- (33) Jorgensen, W. L.; Maxwell, D. S.; Tirado-Rives, J. *J. Am. Chem. Soc.* **1996**, *118*, 11225–11236.
- (34) Kaminski, G. A.; Friesner, R. A.; Tirado-Rives, J.; Jorgensen, W. L. *J. Phys. Chem. B* **2001**, *105*, 6474–6487.
- (35) Pranata, J.; Wierschke, S. G.; Jorgensen, W. L. *J. Am. Chem. Soc.* **1991**, *113*, 2810–2819.
- (36) Hermans, J.; Berendsen, H. J. C.; Van Gunsteren, W. F.; Postma, J. P. M. *Biopolymers* **1984**, *23*, 1513–1518.
- (37) van Gunsteren, W. F.; Berendsen, H. J. C. *Groningen Molecular Simulation (GROMOS) Library Manual*; BIOMOS: Groningen, The Netherlands, 1987.
- (38) Daura, X.; Mark, A. E.; van Gunsteren, W. F. *J. Comput. Chem.* **1998**, *19*, 535–547.
- (39) van Gunsteren, W. F.; Billeter, S. R.; Eising, A. A.; Hünenberger, P. H.; Krüger, P.; Mark, A. E.; Scott, W. R. P.; Tironi, I. G. *Biomolecular Simulation: The GROMOS96 Manual and User Guide*; Verlag der Fachvereine; Zürich, Switzerland, 1996.
- (40) Schuler, L. D.; van Gunsteren, W. F. *Mol. Sim.* **2000**, *25*, 301–319.
- (41) Scott, W. R. P.; Hünenberger, P. H.; Tironi, I. G.; Mark, A. E.; Billeter, S. R.; Fennen, J.; Torda, A. E.; Huber, T.; Krüger, P.; van Gunsteren, W. F. *J. Phys. Chem. A* **1999**, *103*, 3596–3607.
- (42) Schuler, L. D.; Daura, X.; van Gunsteren, W. F. *J. Comput. Chem.* **2001**, *22*, 1205–1218.
- (43) Chandrasekhar, I.; Kastenholz, M.; Lins, R. D.; Oostenbrink, C.; Schuler, L. D.; Tieleman, D. P.; van Gunsteren, W. F. *Eur. Biophys. J.* **2003**, *32*, 67–77.
- (44) Lins, R. D.; Hünenberger, P. H. *J. Comput. Chem.* **2005**, *26*, 1400–1412.
- (45) Soares, T. A.; Hünenberger, P. H.; Kastenholz, M. A.; Kräutler, V.; Lenz, T.; Lins, R. D.; Oostenbrink, C.; van Gunsteren, W. F. *J. Comput. Chem.* **2005**, *26*, 725–737.
- (46) Borjesson, U.; Hünenberger, P. H. *J. Phys. Chem. B* **2004**, *108*, 13551–13559.
- (47) Hansen, H. S.; Hünenberger, P. H. *J. Comput. Chem.* **2010**, *32*, 998–1032.
- (48) Horta, B. A. C.; Fuchs, P. F. J.; van Gunsteren, W. F.; Hünenberger, P. H. *J. Chem. Theory Comput.* **2011**, *7*, 1016–1031.
- (49) Schmid, N.; Eichenberger, A.; Choutko, A.; Riniker, S.; Winger, M.; Mark, A.; van Gunsteren, W. F. *Eur. Biophys. J.* **2011**, *40*, 843–856.



- (50) Hezaveh, S.; Samanta, S.; Milano, G.; Roccatano, D. *J. Chem. Phys.* **2011**, *135*, 164501–11.
- (51) Krautler, V.; Müller, M.; Hunenberger, P. H. *Carbohydr. Res.* **2007**, *342*, 2097–2124.
- (52) Shang, B. Z.; Wang, Z.; Larson, R. G. *J. Phys. Chem. B* **2008**, *112*, 2888–2900.
- (53) Abe, A.; Inomata, K. *J. Mol. Struct.* **1991**, *245*, 399–402.
- (54) Abe, A.; Mark, J. E. *J. Am. Chem. Soc.* **1976**, *98*, 6468–6476.
- (55) Epiotis, N. D.; Sarkanen, S.; Bjorkquist, D.; Bjorkquist, L.; Yates, R. *J. Am. Chem. Soc.* **1974**, *96*, 4075–4084.
- (56) Inagaki, S.; Iwase, K.; Mori, Y. *Chem. Lett.* **1986**, *15*, 417–420.
- (57) Juaristi, E.; Antunez, S. *Tetrahedron* **1992**, *48*, 5941–5950.
- (58) Liu, H.; Mueller-Plathe, F.; van Gunsteren, W. F. *J. Chem. Phys.* **1995**, *102*, 1722–1730.
- (59) Subbotin, O. A.; Sergeyev, N. M. *Anal. Chem.* **1976**, *48*, 545–546.
- (60) Wolfe, S. *Acc. Chem. Res.* **1972**, *5*, 102–111.
- (61) Wolfe, S.; Tel, L. M.; Haines, W. J.; Robb, M. A.; Csizmadia, I. G. *J. Am. Chem. Soc.* **1973**, *95*, 4863–4870.
- (62) Zefirov, N. S.; Gurvich, L. G.; Shashkov, A. S.; Krimer, M. Z.; Vorob'eva, E. A. *Tetrahedron* **1976**, *32*, 1211–1219.
- (63) Zefirov, N. S.; Samoshin, V. V.; Subbotin, O. A.; Baranekov, V. I.; Wolfe, S. *Tetrahedron* **1978**, *34*, 2953–2959.
- (64) Bedrov, D.; Pekny, M.; Smith, G. D. *J. Phys. Chem. B* **1998**, *102*, 996–1001.
- (65) Kolafa, J.; Ratner, M. *Mol. Sim.* **1998**, *21*, 1–26.
- (66) Starovoytov, O. N.; Borodin, O.; Bedrov, D.; Smith, G. D. *J. Chem. Theory Comput.* **2011**, *7*, 1902–1915.
- (67) Smith, G. D.; Jaffe, R. L.; Yoon, D. Y. *J. Phys. Chem.* **1993**, *97*, 12752–12759.
- (68) Smith, G. D.; Borodin, O.; Bedrov, D. *J. Comput. Chem.* **2002**, *23*, 1480–1488.
- (69) Tasaki, K. *J. Am. Chem. Soc.* **1996**, *118*, 8459–8469.
- (70) Neyertz, S.; Brown, D.; Thomas, J. O. *J. Chem. Phys.* **1994**, *101*, 10064–10073.
- (71) Müller-Plathe, F. *Acta Polym.* **1994**, *45*, 259–293.
- (72) Müller-Plathe, F.; van Gunsteren, W. F. *J. Chem. Phys.* **1995**, *103*, 4745–4756.
- (73) Müller-Plathe, F.; van Gunsteren, W. F. *Macromolecules* **1994**, *27*, 6040–6045.
- (74) Anderson, P. M.; Wilson, M. R. *Mol. Phys.* **2005**, *103*, 89–97.
- (75) Anderson, P. M.; Wilson, M. R. *J. Chem. Phys.* **2004**, *121*, 8503–8510.
- (76) Jorgensen, W. L.; Tirado-Rives, J. *J. Am. Chem. Soc.* **1988**, *110*, 1657–1666.
- (77) Fischer, J.; Paschek, D.; Geiger, A.; Sadowski, G. *J. Phys. Chem. B* **2008**, *112*, 2388–2398.
- (78) Stubbs, J. M.; Potoff, J. J.; Siepmann, J. I. *J. Phys. Chem. B* **2004**, *108*, 17596–17605.
- (79) Ferrando, N.; Lachet, V.; Perez-Pellitero, J.; Mackie, A. D.; Malfreyt, P.; Boutin, A. *J. Phys. Chem. B* **2011**, *115*, 10654–10664.
- (80) Ungerer, P.; Beauvais, C.; Delhommelle, J.; Boutin, A.; Rousseau, B.; Fuchs, A. H. *J. Chem. Phys.* **2000**, *112*, 5499–5510.
- (81) Stepniewski, M.; Pasenkiewicz-Gierula, M.; Roig, T.; Danne, R.; Orłowski, A.; Karttunen, M.; Urtti, A.; Yliperttula, M.; Vuorimaa, E.; Bunker, A. *Langmuir* **2011**, *27*, 7788–7798.
- (82) Oostenbrink, C.; Villa, A.; Mark, A. E.; van Gunsteren, W. F. *J. Comput. Chem.* **2004**, *25*, 1656–1676.
- (83) Briggs, J. M.; Matsui, T.; Jorgensen, W. L. *J. Comput. Chem.* **1990**, *11*, 958–971.
- (84) Schmid, N.; Christ, C. D.; Christen, M.; Eichenberger, A. P.; van Gunsteren, W. F. *Comput. Phys. Commun.* **2011**, *183*, 890–903.
- (85) Kunz, A.-P. E.; Allison, J. R.; Geerke, D. P.; Horta, B. A. C.; Hünenberger, P. H.; Riniker, S.; Schmid, N.; van Gunsteren, W. F. *J. Comput. Chem.* **2011**, *33*, 340–353.
- (86) Riniker, S.; Christ, C. D.; Hansen, H. S.; Hünenberger, P. H.; Oostenbrink, C.; Steiner, D.; van Gunsteren, W. F. *J. Phys. Chem. B* **2011**, *115*, 13570–13577.
- (87) Schmid, N.; Allison, J.; Dolenc, J.; Eichenberger, A.; Kunz, A.-P.; van Gunsteren, W. *J. Biomol. NMR* **2011**, *51*, 265–281.
- (88) Eichenberger, A. P.; Allison, J. R.; Dolenc, J.; Geerke, D. P.; Horta, B. A. C.; Meier, K.; Oostenbrink, C.; Schmid, N.; Steiner, D.; Wang, D.; van Gunsteren, W. F. *J. Chem. Theory Comput.* **2011**, *7*, 3379–3390.
- (89) Winger, M.; de Vries, A. H.; van Gunsteren, W. F. *Mol. Phys.* **2009**, *107*, 1313–1321.
- (90) Horta, B. A. C.; Lin, Z.; Huang, W.; Riniker, S.; van Gunsteren, W. F.; Hünenberger, P. H. *J. Comput. Chem.* **2012**, in press.
- (91) Goutev, N.; Ohno, K.; Matsuura, H. *J. Phys. Chem. A* **2000**, *104*, 9226–9232.
- (92) Hess, B.; Kutzner, C.; van der Spoel, D.; Lindahl, E. *J. Chem. Theory Comput.* **2008**, *4*, 435–447.
- (93) Berendsen, H. J. C.; Postma, J. P. M.; van Gunsteren, W. F.; Hermans, J. In *Intermolecular Forces*; Pullman, B., Ed.; Reidel Publishing Company: Dordrecht, The Netherlands, 1981; pp 331–342.
- (94) Hockney, R. W.; Goel, S. P.; Eastwood, J. W. *J. Comput. Phys.* **1974**, *14*, 148–158.
- (95) Hess, B. *J. Chem. Theory Comput.* **2007**, *4*, 116–122.
- (96) Miyamoto, S.; Kollman, P. A. *J. Comput. Chem.* **1992**, *13*, 952–962.
- (97) Berendsen, H. J. C.; Postma, J. P. M.; DiNola, A.; Haak, J. R. *J. Chem. Phys.* **1984**, *81*, 3684–3690.
- (98) Millero, F. J.; Curry, R. W.; Drost-Hansen, W. *J. Chem. Eng. Data* **1969**, *14*, 422–425.
- (99) Fine, R. A.; Millero, F. J. *J. Chem. Phys.* **1973**, *59*, 5529–5536.
- (100) Aicart, E.; Tardajos, G.; Diaz Pena, M. *J. Chem. Eng. Data* **1980**, *25*, 140–145.
- (101) Tironi, I. G.; Sperb, R.; Smith, P. E.; van Gunsteren, W. F. *J. Chem. Phys.* **1995**, *102*, 5451–5459.
- (102) Wohlfahrt, C. In *Numerical Data and Functional Relationships in Science and Technology*; Madelung, O., Ed.; Springer: Berlin, 1991; Vol. 6, pp 5–228.
- (103) Heinz, T. N.; van Gunsteren, W. F.; Hünenberger, P. H. *J. Chem. Phys.* **2001**, *115*, 1125–1136.
- (104) Darden, T.; York, D.; Pedersen, L. *J. Chem. Phys.* **1993**, *98*, 10089–10092.
- (105) Essmann, U.; Perera, L.; Berkowitz, M.; Darden, T.; Lee, H.; Pedersen, L. *J. Chem. Phys.* **1995**, *103*, 8577–8593.
- (106) van Gunsteren, W. F.; Berendsen, H. J. C. *Mol. Sim.* **1988**, *1*, 173–185.
- (107) Parrinello, M.; Rahman, A. *J. Appl. Phys.* **1981**, *52*, 7182–7190.
- (108) Kirkwood, J. G. *J. Chem. Phys.* **1935**, *3*, 300–313.
- (109) Beutler, T. C.; Mark, A. E.; van Schaik, R. C.; Gerber, P. R.; van Gunsteren, W. F. *Chem. Phys. Lett.* **1994**, *222*, 529–539.
- (110) Dormidontova, E. E. *Macromolecules* **2004**, *37*, 7747–7761.
- (111) Flory, P. J. *Statistical Mechanics of Chain Molecules*; John Wiley & Sons: New-York, 1969.
- (112) Waggoner, R. A.; Blum, F. D.; Lang, J. C. *Macromolecules* **1995**, *28*, 2658–2664.
- (113) Yoshida, H.; Matsuura, H. *J. Phys. Chem. A* **1998**, *102*, 2691–2699.
- (114) Funasaki, N.; Hada, S.; Neya, S.; Machida, K. *J. Phys. Chem.* **1984**, *88*, 5786–5790.
- (115) Chen, B.; Siepmann, J. I. *J. Phys. Chem. B* **2006**, *110*, 3555–3563.
- (116) Samanta, S.; Hezaveh, S.; Milano, G.; Roccatano, D. *J. Phys. Chem. B* **2012**, *116*, 5141–5151.
- (117) Stuart, M. A. C.; Waajen, F. H. W. H.; Cosgrove, T.; Vincent, B.; Crowley, T. L. *Macromolecules* **1984**, *17*, 1825–1830.
- (118) Devanand, K.; Selser, J. C. *Macromolecules* **1991**, *24*, 5943–5947.
- (119) Mark, J. E.; Flory, P. J. *J. Am. Chem. Soc.* **1965**, *87*, 1415–1423.
- (120) Kawaguchi, S.; Imai, G.; Suzuki, J.; Miyahara, A.; Kitano, T.; Ito, K. *Polymer* **1997**, *38*, 2885–2891.
- (121) Bower, D. I. *An Introduction to Polymer Physics*; Cambridge University Press: Cambridge ; New York, 2002.



- (122) Kienberger, F.; Pastushenko, V. P.; Kada, G.; Gruber, H. J.; Riener, C.; Schindler, H.; Hinterdorfer, P. *Single Mol.* **2000**, *1*, 123–128.
- (123) de Gennes, P. G. *Introduction to Polymer Dynamics*; Cambridge University Press: New York, 1990.
- (124) Strobl, G. R. *The Physics of Polymers: Concepts for Understanding Their Structures and Behavior*; Springer: Berlin, 1996.
- (125) Deechongkit, S.; Dawson, P. E.; Kelly, J. W. *J. Am. Chem. Soc.* **2004**, *126*, 16762–16771.
- (126) Kabsch, W.; Sander, C. *Biopolymers* **1983**, *22*, 2577–2637.
- (127) *The PyMOL Molecular Graphics System*, Version 1.3r.1; Schrödinger, LLC: 2010.
- (128) Jorgensen, W. L.; Chandrasekhar, J.; Madura, J. D.; Impey, R. W.; Klein, M. L. *J. Chem. Phys.* **1983**, *79*, 926–935.
- (129) Lamoureux, G.; MacKerell, J. A. D.; Roux, B. *J. Chem. Phys.* **2003**, *119*, 5185–5197.
- (130) Horn, H. W.; Swope, W. C.; Pitner, J. W.; Madura, J. D.; Dick, T. J.; Hura, G. L.; Head-Gordon, T. *J. Chem. Phys.* **2004**, *120*, 9665–9678.
- (131) Berendsen, H. J. C.; Grigera, J. R.; Straatsma, T. P. *J. Phys. Chem.* **1987**, *91*, 6269–6271.
- (132) Guvench, O.; Greene, S. N.; Kamath, G.; Brady, J. W.; Venable, R. M.; Pastor, R. W.; Mackerell, A. D. *J. Comput. Chem.* **2008**, *29*, 2543–2564.
- (133) Hezaveh, S.; Samanta, S.; Milano, G.; Roccatano, G. *J. Chem. Phys.* **2012**, *136*, 124901.

#### ■ NOTE ADDED IN PROOF

The experimental and calculated values of  $\log_{10}(P_{OW})$  for DXE quoted in ref 116 indeed had the wrong sign and a corrigendum to this article has now been published. The results of ref 116, the present results, and the experiment thus consistently indicate a preferential affinity of DXE for water compared to octanol.